AIAA JOURNAL
Vol. 47, No. 12, December 2009

Physics-Based Foundation for Empirical Mode Decomposition

Young S. Lee*
New Mexico State University, Las Cruces, New Mexico 88003
Stylianos Tsakirtzis†
National Technical University of Athens, 157 80 Athens, Greece
and
Alexander F. Vakakis,‡ Lawrence A. Bergman,§ and D. Michael McFarland¶
University of Illinois at Urbana–Champaign, Urbana, Illinois 61801

DOI: 10.2514/1.43207

We study the correspondence between analytical and empirical slow-flow analyses. Given a sufficiently dense set of sensors, measured time series recorded throughout a mechanical or structural system contains all information regarding the dynamics of that system. Empirical mode decomposition is a useful tool for decomposing the measured time series in terms of intrinsic mode functions, which are oscillatory modes embedded in the data that fully reproduce the time series. The equivalence of responses of the analytical slow-flow models and the dominant intrinsic mode functions derived from empirical mode decomposition provides a physics-based theoretical foundation for empirical mode decomposition, which currently is performed formally in an ad hoc fashion. To demonstrate correspondence between analytical and empirical slow flows, we derive appropriate mathematical expressions governing the empirical slow flows and based on analyticity conditions. Several nonlinear dynamical systems are considered to demonstrate this correspondence, and the agreement between the analytical and empirical slow dynamics proves the assertion.

I. Introduction

SIGNAL processing is concerned with the mathematical representation of a signal and the algorithmic operations performed on it to extract the information it carries. The method of information extraction depends on the type of signal and the nature of the information being carried by it [1].

There are numerous signal-processing techniques to decompose a signal into a set of simple intrinsic oscillators, among which the so-called empirical mode decomposition (EMD) is the simplest. The objective of this study is not only to demonstrate improvement of the EMD method itself by using masking and mirror-image signals, but also to establish the physical meaning of the decomposed intrinsic oscillators by means of an analytical tool based on the complexification-averaging technique. This will provide a physics-based theoretical foundation for EMD.

Slow-flow dynamics is a useful tool for understanding the major features of a (nonlinear) dynamical system. The slow-flow model for a dynamical process is derived by introducing a slow/fast partition of the dynamics whereby the nonessential fast dynamics is averaged out to reveal the important slow-flow modulations of amplitudes and phases. To extract slowly varying system quantities, numerous perturbation tools have been developed. Examples are the method of direct series expansion (e.g., the Linstedt method), the method of multiple scales, the harmonic balance method [2], the averaging theorem [3], and others. Focusing more on transient dynamical phenomena, the complexification-averaging technique [4,5] recently has received much attention due to its capacity to provide slow-flow models even for strongly nonlinear dynamical interactions; for example, of resonance capture phenomena in coupled oscillators with essentially nonlinear attachments [6,7]. In the limit of very lightweight nonlinear attachments, the idea of singular perturbations [8] can be employed for partitioning the dynamics into slow and fast time scales.

In analyzing a time series obtained from measurements or numerical simulations, potential problems include short total data span, nonstationarity, and nonlinearity of the data. Fourier spectral analysis, which is probably the most popular signal analysis tool, assumes linearity and stationarity in the data and exhibits spurious harmonic components even for a pure harmonic signal. This spurious feature of time-frequency analysis yields a misleading energy-frequency distribution.

The wavelet transform, which is a popular time-frequency analysis tool, involves a windowing technique with variable-sized regions so that it performs a multiresolution analysis; small time intervals are considered for high-frequency components, whereas the size of the interval is increased for lower-frequency components, thereby giving better time and frequency resolutions than the Fourier analysis [9]. Nonetheless, the wavelet analysis is not free of misleading energy-frequency distribution because, in essence, it is still based upon Fourier analysis. In this section, we discuss how the use of EMD can overcome such drawbacks in time-frequency analysis.

Because the EMD (or standard EMD) of time series was introduced by Huang et al. [10–12], numerous applications of it have been examined; for example, in system identification problems [13–15], damage detection, and health monitoring [16–20]. The motivation for performing EMD is to decompose nonstationary and nonlinear data into a set of simple and intrinsic oscillations at the characteristic time scales of the dynamics in an ad hoc manner requiring no a priori system information. Such decomposition based on the local characteristic time scale of the data is adaptive and highly efficient so that it becomes suitable for nonlinear and nonstationary

---

Received 13 January 2009; revision received 6 July 2009; accepted for publication 18 August 2009.

*Assistant Professor, Department of Mechanical and Aerospace Engineering; younglee@nmsu.edu. Member AIAA.

†Research Associate, School of Applied Mathematical and Physical Sciences; tsakstel@central.ntua.gr.

‡Professor, Department of Mechanical Science and Engineering; avakakis@illinois.edu.

§Professor, Department of Aerospace Engineering; lbergman@illinois.edu. Associate Fellow AIAA.

¶Research Associate Professor, Department of Aerospace Engineering; dmmcf@illinois.edu. Senior Member AIAA.

processes. Thus, application of EMD to a given time series yields a set of the so-called intrinsic mode functions (IMFs), and this set of IMFs forms a complete and almost orthogonal basis for the time series [10].

However, as has been addressed in many studies (see, for example, Chen and Feng [21], Flandrin et al. [22], Peng et al. [23], Yang [24], and Wu and Huang [25]), there exist some limitations in the standard EMD analysis, such as lack of orthogonality (or spuriousness of the resulting IMFs) and difficulties in decomposing closely spaced modes. To overcome such drawbacks of the standard EMD, many supplementary techniques have been investigated. Yang [24] used an adaptive bandpass filter for preprocessing before applying EMD. Peng et al. [23] improved EMD with the help of the wavelet packet transform as a preprocessor to decompose a signal into a set of narrowband signals before applying EMD. Chen and Feng [21] studied the decomposition of narrowband signals based on wave beating phenomena. Similarly, Senroy et al. [26] implemented masking signals [27] based on fast Fourier transforms to separate components with closely spaced frequencies; the decomposition was compared with the results obtained by the *S*-transform, which is a phase-corrected wavelet transform. Flandrin et al. [22] examined EMD as a dyadic filter bank resembling those involved in wavelet decompositions, and then Wu and Huang [25] developed an ensemble EMD consisting of sifting an ensemble of white noise-added signals and treating the mean as the final result.

Several efforts were recently made to use the IMFs for slow-flow model identification [28,29]. The proposed method was applied to characterize and estimate system parameters for a mathematical model or an experimental multidegree-of-freedom coupled oscillator. We expand this idea in this work to establish an analytical equivalence between analytical and empirical slow-flow analyses. For this purpose, the analytical method for deriving a slow-flow model using the method of complexification averaging (CX-A), and an enhanced version of EMD, are discussed in Sec. II and III respectively. In particular, the enhanced EMD method makes use of masking signals to greatly enhance the frequency resolution of the decomposition, as well as mirror-image signals that nullify the end effects while having no other influences on the transformation of the original time series. In Sec. IV, the analyticity properties of the IMFs are investigated and certain relevant examples are discussed in Sec. V. The equivalence between the analytical and empirical slow-flow analyses discussed in this paper form the theoretical foundation for a new nonparametric nonlinear system identification method, which is further investigated in another paper [30].

II. Slow-Flow Model by Complexification Averaging

As a preliminary example of a slow-flow model we consider a simple pendulum with slowly varying length, approximated as the Duffing equation with time-varying coefficients [31],

$$\frac{\mathrm{d}}{\mathrm{d}t}[l^2(\tau)\dot{u}(t)] + gl(\tau)u(t) - \frac{\epsilon}{6}gl(\tau)u^3(t) = 0 \tag{1}$$

where $\dot{()} = \mathrm{d}/\mathrm{d}t$, and $\tau = \epsilon t(\epsilon \ll 1)$ is a slow-time scale. The slowly varying amplitude $a(\tau)$ and frequency $\omega(\tau)$ of the pendulum can be approximated as [31]

$$a(\tau) = a(0)\left[\frac{l(0)}{l(\tau)}\right], \qquad \omega(\tau) = \sqrt{\frac{g}{l(\tau)}}\left\{1 - \frac{\epsilon}{16}a^2(0)\left[\frac{l(0)}{l(\tau)}\right]\right\} \tag{2}$$

Figure 1 depicts a typical response when $l(\tau) = l(0)(1 + \epsilon \sin\tau)$, $\epsilon = 0.15$, $l(0) = 10$, and $a(0) = 1$. The simple pendulum of constant length (i.e., $l(\tau) = l_0 = \text{constant}$) will exhibit a periodic motion with constant amplitude $a(0)$ and constant (fast) frequency $\omega_0 = \sqrt{g/l_0}[1 + \epsilon a(0)^2/16]$. On the other hand, the pendulum with time-varying length will possess a time-varying amplitude $a(\tau)$ and time-varying frequency $\omega(\tau)$. Its response can then be expressed as $u(t) \approx a(\tau)\exp[j\omega(\tau)] = a(\tau)\exp[\omega_0 t + \phi(\tau)]$, where the slowly varying phase is computed by the expression

$$\phi(\tau) = -\epsilon a(0)^2/16 \int_0^\tau \sqrt{g/l(s)}[l(0)/l(s)]\mathrm{d}s$$

The amplitude modulations then represent the slow oscillation $a(\tau)\exp[j\phi(\tau)]$, and the important dynamics are captured by this slow oscillation rather than by the fast oscillation $\exp[j\omega_0 t]$ where $j^2 = -1$.

For generalization of this idea, we consider an n-degree-of-freedom (DOF) nonlinear dynamical system in the general form,

$$\dot{\mathbf{X}} = \mathbf{f}(\mathbf{X}, t), \qquad \mathbf{X} = \{\,\mathbf{x}^T \quad \dot{\mathbf{x}}^T\,\}^T \in \mathbb{R}^{2n}, \qquad t \in \mathbb{R} \tag{3}$$

where $\mathbf{x}$ and $\dot{\mathbf{x}}$ are the displacement and velocity vectors, respectively. To establish an analytical slow-flow model for this system, we employ the CX-A technique [4,5], which is briefly discussed here.

Assume that the dynamics of interest contains N distinct components at frequencies, $\omega_1, \omega_2, \ldots, \omega_N$, so that the response at each

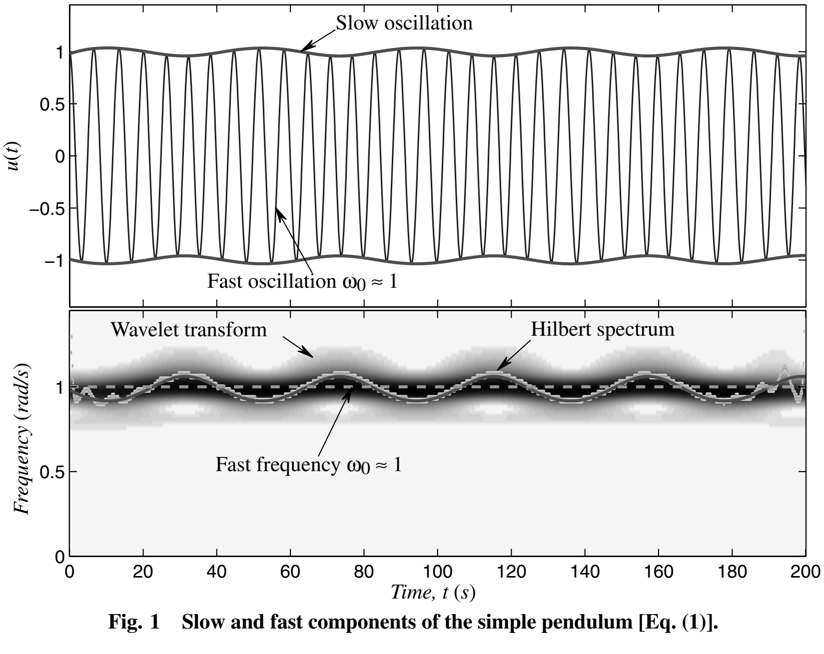

Fig. 1 Slow and fast components of the simple pendulum [Eq. (1)].

DOF of the system can be expressed as the sum of N independent components

$$x_k(t) = x_k^{(1)}(t) + x_k^{(2)}(t) + \cdots + x_k^{(N)}(t), \qquad k = 1, 2, \ldots, n \quad (4)$$

where $x_k^{(m)}(t)$, $m = 1, 2, \ldots, N$, indicates the component of the response of the kth coordinate associated with frequency ω_m, with the ordering $\omega_1 < \omega_2 < \cdots < \omega_N$.

It turns out that even strongly nonlinear dynamical processes can be analyzed by an analytical technique termed CX-A, first introduced by Manevitch [5] (for an extensive discussion of this technique and numerous applications refer to Vakakis et al. [32]). In particular, for each frequency component in (4) we introduce a new complex variable defined by

$$\psi_k^{(m)}(t) = \dot{x}_k^{(m)}(t) + j\omega_m x_k^{(m)}(t) \triangleq \varphi_k^{(m)}(t) e^{j\omega_m t} \quad (5)$$

where $\varphi_k^{(m)}(t) \in \mathbb{C}$, $k = 1, \ldots, n$, and $e^{j\omega_m t}$ represent the slow and fast components, respectively, of the mth fast-frequency component of the response of the kth coordinate. It is clear that the real dependent variables and their time derivatives can be expressed in terms of the new complex variables as

$$x_k^{(m)}(t) = \frac{1}{2j\omega_m}[\psi_k^{(m)}(t) - \psi_k^{(m)*}(t)]$$
$$\dot{x}_k^{(m)}(t) = \frac{1}{2}[\psi_k^{(m)}(t) + \psi_k^{(m)*}(t)] \quad (6)$$

where $()^*$ denotes complex conjugate.

In the presence of multiple frequency components, the method of multiphase averaging [33] can be used to perform fast–slow partitioning of the dynamics. Substituting into Eq. (3), and averaging out the fast-frequency components other than $e^{j\omega_m t}$, $m = 1, 2, \ldots, N$, we obtain the slow-flow model in the form

$$\dot{\Phi}_k = \mathbf{F}_k(\Phi_k), \qquad \Phi_k \in \mathbb{C}^N \quad (7)$$

where $\Phi_k = \{\varphi_k^{(1)}, \varphi_k^{(2)}, \ldots, \varphi_k^{(N)}\}^T$, $k = 1, 2, \ldots, n$. We note that the dimension N of this slow-flow model may exceed the number of degrees of freedom of the original dynamical system, because the number of fast frequencies is what determines its dimensionality. There are numerous papers that use this method (see, for example, Vakakis and Gendelman [7] and others [34–36]), and some examples will be discussed in Sec. V.

III. Empirical Mode Decomposition

A. Standard Empirical Mode Decomposition Method

The motivation for the EMD is to decompose a nonstationary and nonlinear time series into a set of intrinsic oscillatory functions at different time scales of the dynamics in an ad hoc manner requiring no a priori system information. Such decomposition based on the local characteristic time scales of the data is adaptive and highly efficient, so it becomes suitable for nonlinear and nonstationary processes. Thus, application of the EMD to a given time series yields a set of so-called IMFs, which form a complete and almost orthogonal basis for the time series [10].

In order for a function $c(t)$ to be considered an IMF, it must satisfy the following two basic properties: 1) it must possess exactly one zero between any two consecutive local extrema; and 2) it must have zero local mean. A function that satisfies only condition 1 is called a weak IMF. A complete characterization of weak IMFs can be performed in terms of solutions of self-adjoint ordinary differential equations, which usually arise from mechanical vibration problems; moreover, any modification of the definition of an IMF must necessarily include the condition 1 for a weak IMF [37].

The main loop of the algorithm for extracting the IMFs of a signal $x(t)$ (i.e., the standard EMD procedure) is summarized as follows [10,38]: 1) identify all extrema of $x(t)$; 2) perform (spline-) interpolations between minima (maxima), resulting in an envelope $e_{\min}(t)$ [$(e_{\max}(t))$]; 3) compute the average $R(t) = [e_{\min}(t) + e_{\max}(t)]/2$ (considered as a residual); 4) extract the detail $c(t) = x(t) - R(t)$; and 5) iterate on the residual $R(t)$. In practice, the EMD procedure is refined by a sifting process, and the inner loop that iterates 1–4 on the detail $c(t)$ runs until the average $R(t)$ can be considered zero-mean under some tolerance (i.e., as a stopping criterion). Once achieved, the detail $c(t)$ is regarded as the effective IMF. This procedure will be hereafter called the standard EMD method (SEMD).

Suppose that the response of the kth DOF of a discrete dynamical system, $x_k(t)$, can be decomposed into N components (i.e., N dominant IMFs) resulting in the decomposition

$$x_k(t) \approx c_1^{(k)}(t) + c_2^{(k)}(t) + \cdots + c_N^{(k)}(t), \qquad k = 1, 2, \ldots, n \quad (8)$$

where the residual is neglected and $c_m^{(k)}(t)$, $m = 1, 2, \ldots, N$, indicates the component associated with the dominant frequency ω_m. By construction the application of EMD yields IMFs sequentially from higher to lower frequency components, so that a formal multiscale decomposition of the dynamics is performed. Moreover, we adopt notation similar to that used in Sec. II; that is, that the IMF with the larger subscript is the higher-frequency component. This convention will be useful when considering the equivalence of the analytical and empirical slow flows in Sec. IV.

To check the orthogonality of the IMFs used in the decomposition of the signal (8) we compute its square,

$$x_k^2(t) \approx \sum_{i=1}^{N}[c_i^{(k)}(t)]^2 + 2\sum_{m=1}^{N}\sum_{l=1}^{N} c_l^{(k)}(t) c_m^{(k)}(t) \quad (9)$$

Then, the overall index of orthogonality [10] for the decomposition (8) is defined by considering the relative magnitudes of the cross terms in the second part of (9).

$$\mathrm{IO}_k \triangleq \sum_{t=0}^{T}\left[\sum_{m=1}^{N}\sum_{l=1}^{N} c_l^{(k)}(t) c_m^{(k)}(t)/x_k^2(t)\right] \quad (10)$$

If the decomposition yields completely orthogonal IMFs or if the signal is an IMF itself, then the index of orthogonality should be zero. Moreover, the closer index of orthogonality is to zero, the better the orthogonality between the IMFs is. The quantification of the degree of orthogonality between IMFs provided by the index (10) paves the way for optimizing the extracted basis of IMFs to ensure minimization of the orthogonality index. In view of the well-known nonuniqueness of EMD results, the basis of IMFs corresponding to the least value of index of orthogonality (typically, on the order of 10^{-3}) in this study will be regarded as forming a reasonably orthogonal basis for the signal.

As a demonstration, the SEMD analysis is performed on the signal

$$x(t) = A_1 \sin 2\pi f_1 t + A_2 \sin 2\pi f_2 t + A_3 \sin 2\pi f_3 t$$

, where $A_1 = 1$, $A_2 = 0.5$, $A_3 = 0.7$ and $f_1 = 1$, $f_2 = 3f_1$, $f_3 = 5f_1$ (Hz).** The left column of Fig. 2 presents the schematic of the SEMD procedure, where the exact decomposition should yield $c_i(t) = A_i \sin(2\pi f_i t)$, $i = 1, 2, 3$. The gray lines indicate the original signal and the residual obtained at each step; the black lines represent the extracted components as the mean of local extrema, sequentially obtained from the higher- to lower-order harmonics (i.e., from f_3 to f_1). The squares (circles) are the local minima (maxima), and the dashed lines represent the spline interpolations through those local maxima and minima, respectively. To study the frequencies of the computed IMFs, the wavelet transform spectrum of each IMF is plotted on the right column of Fig. 2, where the Matlab codes developed by Dr. V. Lenaerts (Université de Liège, Belgium) in collaboration with Dr. P. Argoul (Ecole Nationale des Ponts et Chaussées, France) were used, and the Morlet wavelet, which is a Gaussian-windowed complex sinusoid, is considered as the mother wavelet here (see, for example, Argoul and Le [39,40]).

**The time steps used in this study are $\Delta t = 0.01$ and $\Delta t = 0.1$ (s) in this section and Sec. V, respectively.

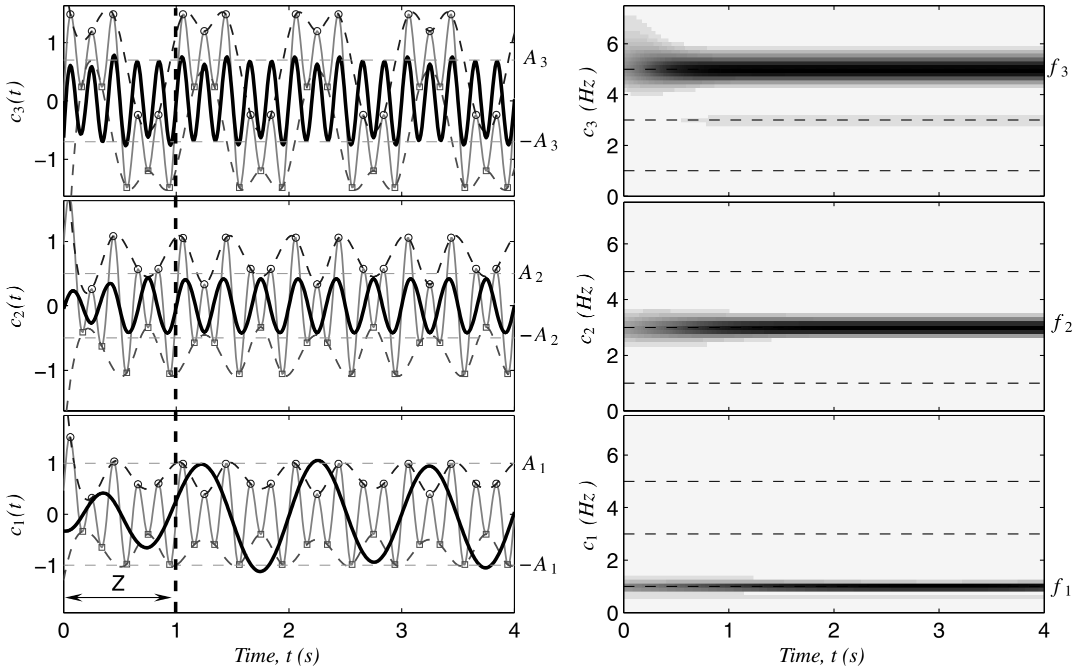

Fig. 2 SEMD analysis of the signal of $x(t) = \sum_{k=1}^{3} A_k \sin(2\pi f_k t)$, where $A_1 = 1, A_2 = 0.5, A_3 = 0.7$, and $f_1 = 1, f_2 = 3, f_3 = 5$ (Hz): IMFs from the EMD analysis, and corresponding wavelet transform spectra; in the interval Z end effects occur due to the Gibbs phenomenon during interpolation.

It is clear that the SEMD can extract the three distinct frequency components (which are well-spaced from each other) and the envelopes of the amplitudes from the original signal, which is simply a linear combination of harmonics. The end effects in the initial period (due to the Gibbs phenomenon; also known as ringing artifacts), as in other time-frequency analyses, are prominent in the interval Z in Fig. 2. These end effects appear in the form of overshoots, which is a consequence of trying to approximate a discontinuous function with a partial (i.e., finite) sum of continuous functions; in addition, there exist numerical artifacts due to the computational Hilbert transform, and also those caused by spline interpolation during the sifting process (see, for example, Delechelle et al. [41]).

In spite of the nice decomposition in the previous demonstration, the SEMD method is often incapable of generating a set of proper IMFs. By a proper IMF we mean an IMF that is monocomponent or narrowband so that it becomes suitable for Hilbert transformation. As mentioned previously, SEMD does not provide a unique decomposition of a signal and strongly depends on a free stopping parameter; that is, the decomposition is not robust in practice, particularly when the signal is the output of a strongly nonlinear transient dynamical process. Furthermore, it fails to extract high-frequency components hidden in a signal containing inflectionlike points (see the discussion in Sec. III.B).

When a set of IMFs is considered as a basis for decomposing a signal (time series), it should be examined in terms of completeness and orthogonality. Completeness is guaranteed by virtue of the decomposition, and can be verified by reconstructing the original signal as the sum of all IMFs. However, spuriousness of the IMFs cannot be avoided in many applications, which in turn is a consequence of the fact that the resulting IMFs form (in general) a nonorthogonal basis. Huang et al. [10] argued that locality and adaptivity are the necessary conditions for an IMF basis for expanding nonlinear and nonstationary time series, whereas orthogonality is not a necessary criterion for the basis selection, restricting its requirement only to linear decomposition systems.

Despite this argument, we believe that multifrequency components (or mode-mixing) in an IMF prevents a proper understanding of nonstationary nonlinear dynamical processes, so orthogonality (or near orthogonality) should be a crucial factor for a set of IMFs, as this would minimize spuriousness of the basis and contribute toward a physics-based foundation of EMD. This can be performed by selecting the IMF basis corresponding to a minimal index of orthogonality (typically, $\mathcal{O}(10^{-3})$), so this will be the selected criterion for improving EMD in this study. This will require an enhancement of the EMD procedure through the use of masking and mirror-image signals, leading to an advanced EMD (AEMD) method as described in the next section.

B. The Advanced Empirical Mode Decomposition Method

To overcome the aforementioned drawbacks of the standard EMD, many supplementary techniques have been investigated [21–25]. Although the improvement methods for EMD performance employ similar principles, in this study we adopt the use of masking signals with the Matlab codes developed by Rilling et al. [38]. Furthermore, we employ mirror-image signals in our time-frequency analysis to nullify the numerical artifacts in the initial transients of the signal reconstruction. To make a distinction from the standard EMD, our suggested enhanced method will be referred to as the AEMD method. One of the main objectives of the AEMD is to generate a set of IMFs that are monocomponent or narrowband and form an almost orthogonal basis for the signal.

1. Narrowbandedness of an Intrinsic Mode Function

By definition, a proper IMF should be monocomponent or narrowband. A truly monocomponent signal can be represented as $e^{j\omega_m t}$ with a constant amplitude, whereas a narrowband IMF is a signal with slow amplitude modulations whose dominant frequencies lie within a certain bandwidth. As discussed in the Appendix, the narrowbandedness of a signal is defined by the ratio of its dominant frequencies; in practical terms, when this ratio lies roughly within [0.5, 2], the signal may be said to be narrowband. EMD analysis will suffer difficulties in decomposing these frequency components, even if they are clearly distinct. This is the case not only for the SEMD, but also for our suggested AEMD as well. The issue of analyzing and modeling signals with closely spaced modes will be left for future work, and herein we will be concerned only with time series that possess distinct dominant frequencies.

2. Expansion with Mirror-Image Signals

The idea of expanding a time series by adding to it its mirror image is due to the observation that the numerical artifacts in decomposition and time-frequency analysis become prominent only near the initial and final time intervals of the time window considered (hence, they are called end effects). Such end effects in the initial period of the reconstruction of a time series might blur interpretation of interesting dynamical phenomena occurring during the initial transients. In addition, they might interfere with the determination of the proper initial conditions for a multiphase-averaged system based on the equivalence between the analytical and empirical slow flows (see Sec. IV for more discussion).

Denote the original time series by $x(t)$, $t \in [0, t_f]$; then its mirror-image signal is defined by $x_{\text{mirror}}(t)$, $t \in [-t_f, 0)$, and the expanded signal, by $\hat{x}(t) = \{x_{\text{mirror}}(t);\quad x(t)\}^T$, $t \in [-t_f, t_f]$. A rule of thumb for an expansion with a mirror-image signal is that the mirror image must preserve smoothness in the instantaneous frequency of the expanded signal at the symmetry point so that the expanded signal is continuously differentiable at that point (i.e., $\hat{x}(t) \in C^1$ for $t \in (0_-, 0_+)$). The most convenient symmetry is when an even expansion $x_{\text{mirror}}(t) = x(-t)$ is selected, when $\dot{x}(t)|_{t=0_+} = 0$; otherwise an odd expansion $x_{\text{mirror}}(t) = -x(-t)$ is considered.

In practice, we apply the following condition for a mirror-image signal

$$x_{\text{mirror}}(t) = \begin{cases} x(-t), & \text{for } |\dot{x}(t)|_{t=0_+} < \epsilon \\ -x(-t), & \text{otherwise} \end{cases} \tag{11}$$

where ϵ is a small positive number. The evaluation of the derivative at $t = 0^+$ is subject to the usual numerical difficulties, and care must be taken to use a small step size, filter high-frequency noise, and so forth in its computation.

Once all the calculations (such as wavelet or Hilbert transformations or empirical decompositions) have been performed, the portion of the time series corresponding to the mirror-image signal is discarded from the final result.

As a demonstration time-frequency analyses of $x(t) = \sin(6\pi t)$ and $x(t) = \cos(6\pi t)$ are presented in Figs. 3a and 3b, respectively. Because the sine function is odd (i.e., symmetric with respect to the origin; $x(t) = -x(-t)$), it is natural to complement it with its mirror-image signal by performing an odd expansion. In Fig. 3a the usefulness of adding the mirror-image signal is clear from the absence of numerical artifacts in the wavelet transform spectrum of the expanded signal.

On the other hand, the cosine function requires a mirror-image signal created by even expansion due to the symmetry of the original signal with respect to $t = 0$; i.e., $x(t) = x(-t)$. In Fig. 3b, the wavelet transform spectra of odd- and even-expanded functions are compared for this case. Whereas the odd expansion yields serious numerical artifacts present over the entire time domain as very low-frequency components, the even expansion completely nullifies the end effects even during the initial period of the wavelet spectrum.

If necessary, the expansion with a mirror-image signal can also be applied at the end time interval to obtain clean time-frequency behavior over the entire time domain. However, in this work we will restrict application of a mirror-image signal to only the initial regime of the response because in many applications the early-time intervals are the most highly energetic, and so it is in these intervals where strongly nonlinear dynamical effects take place. Moreover, a mirror-image signal can be applied not only for time-frequency analysis, but also for EMD analysis. The need for employing mirror-signal techniques in EMD is dictated by the requirement that, by construction, the sum of initial conditions of all (dominant) IMFs of the signal should be equal to, or at least nearly equal to, the initial conditions of the original time series. That is, the decomposition of the kth DOF response should satisfy the relationship

$$x_k(0) \approx \sum_{m=1}^{n_e} c_m^{(k)}(0)$$

where $n_e \leq N$ is the number of dominant IMFs.

3. *Using Masking Signals*

The use of a masking signal in EMD resulted from the problems of intermittency, mode mixing, or closely spaced modes [26,27]. Although there are still certain limitations in decomposing closely spaced modes even with the AEMD method (cf. Appendix), we restrict our interest to the case where the original time series possesses distinct components whose frequency contents are in ratio outside the range [0.5, 2].

The role of a masking signal in EMD can be interpreted in two ways. First, incorporating a masking signal (usually with a harmonic higher than the highest frequency in the original time series) into the original time series introduces randomness in the EMD algorithm. The high-frequency content in the masking signal then acts as noise during decomposition (see, for example, Flandrin et al. [22]), and provides robustness to the EMD to yield a set of proper IMFs. Second, tuning a masking signal to the highest-frequency component of the original time series amplifies this highest-frequency component (in particular, when it is weak and buried compared with the other harmonics) so that EMD analysis may yield clear separation of the highest-frequency component and, sequentially, of the lower components. In all cases, the primary goal of applying a masking signal is the clear identification and decomposition of the highest-frequency component of the time series.

A masking signal frequently takes the form of a simple harmonic function; that is, we often employ a masking signal of the form $x_{\text{mask}}(t) = \bar{a} \sin \bar{\omega} t + \bar{b} \cos \bar{\omega} t$. The choice of the amplitudes, $\bar{a}$, $\bar{b}$, and frequency, $\bar{\omega}$, is purely empirical and nonunique. One can also refer to the criteria suggested in Senroy et al. [26], and Deering and Kaiser [27].

As a demonstration, AEMD is performed on the time series depicted in Fig. 4a. From the waveform of the signal, we may infer from the beginning that the time series $x(t) = \cos(2\pi f_1 t) + 0.3\cos(2\pi f_2 t)$, where $f_1 = 1$ and $f_2 = 3$ (Hz), in Fig. 4a satisfies all conditions for an IMF (see Sec. III.A). Thus, the SEMD will never separate the hidden high-frequency component of the signal, which manifests itself in the form of inflection points at quarter- or three-quarter-period intervals. Figure 4b presents the two IMFs extracted with the help of a masking signal $x_{\text{mask}}(t) = 0.5 x_{\max} \cos(2\pi \bar{f} t)$, $\bar{f} = f_1 + f_2$. The choice of the masking frequency $\bar{f}$ is due to Senroy et al. [26], and the cosine function is selected to produce an in-phase initial condition between $x(t)$ and $x_{\text{mask}}(t)$. Using a mirror-image signal provides a set of two IMFs with clear separation of components (index of orthogonality $= 1.65 \times 10^{-3}$) and no end effects in the initial stage of the signal (Fig. 4c). Also, completeness of the basis of the two IMFs can be verified by comparing $x(t)$ with the reconstructed signal $c_1(t) + c_2(t)$, which is depicted in Fig. 4d. The normalized mean square error between the envelopes of $x(t)$ and $c_1(t) + c_2(t)$ is computed as $4.68 \times 10^{-3}\%$.

A different masking signal $x_{\text{mask}}(t) = 0.4 x_{\max} \cos(2\pi \bar{f} t)$, $\bar{f} = 20 f_1$, is considered in Fig. 5 to demonstrate how the masking signal works in separating different components of the time series in Fig. 4a. The masking frequency in this case is approximately 7 times higher than f_2, and hence the resulting masking signal acts as noise in the original time series. The use of the masking signal is described as follows [27]. First, perform EMD analysis for the signal $x(t) + x_{\text{mask}}(t)$ to yield the IMFs denoted by $c_0^+(t)$, $c_2^+(t)$, and $c_1^+(t)$ (left column of Fig. 5a); then, perform EMD analysis of the signal $x(t) - x_{\text{mask}}(t)$, yielding the IMFs $c_0^-(t)$, $c_2^-(t)$, and $c_1^-(t)$ (right column of Fig. 5a). Then, compute the means of the respective IMFs to eliminate the influence of the masking signal in the EMD results; that is, compute $c_0(t) = [c_0^+(t) + c_0^-(t)]/2$, $c_1(t) = [c_1^+(t) + c_1^-(t)]/2$, and $c_2(t) = [c_2^+(t) + c_2^-(t)]/2$. Apparently, the IMFs $c_0^{\pm}(t)$ correspond to the components of the masking signal at frequency $\bar{f} = 20 f_1$, which are out of phase to each other; therefore, averaging these two IMFs results in almost zero mean values over the whole time span, which implies that the effects of the masking signal are almost completely eliminated from further analysis (Fig. 5b). The remaining averaged IMFs $c_1(t)$ and $c_2(t)$ become the physically meaningful decompositions with frequency components f_1 and f_2, which are the same as those in Fig. 4b.

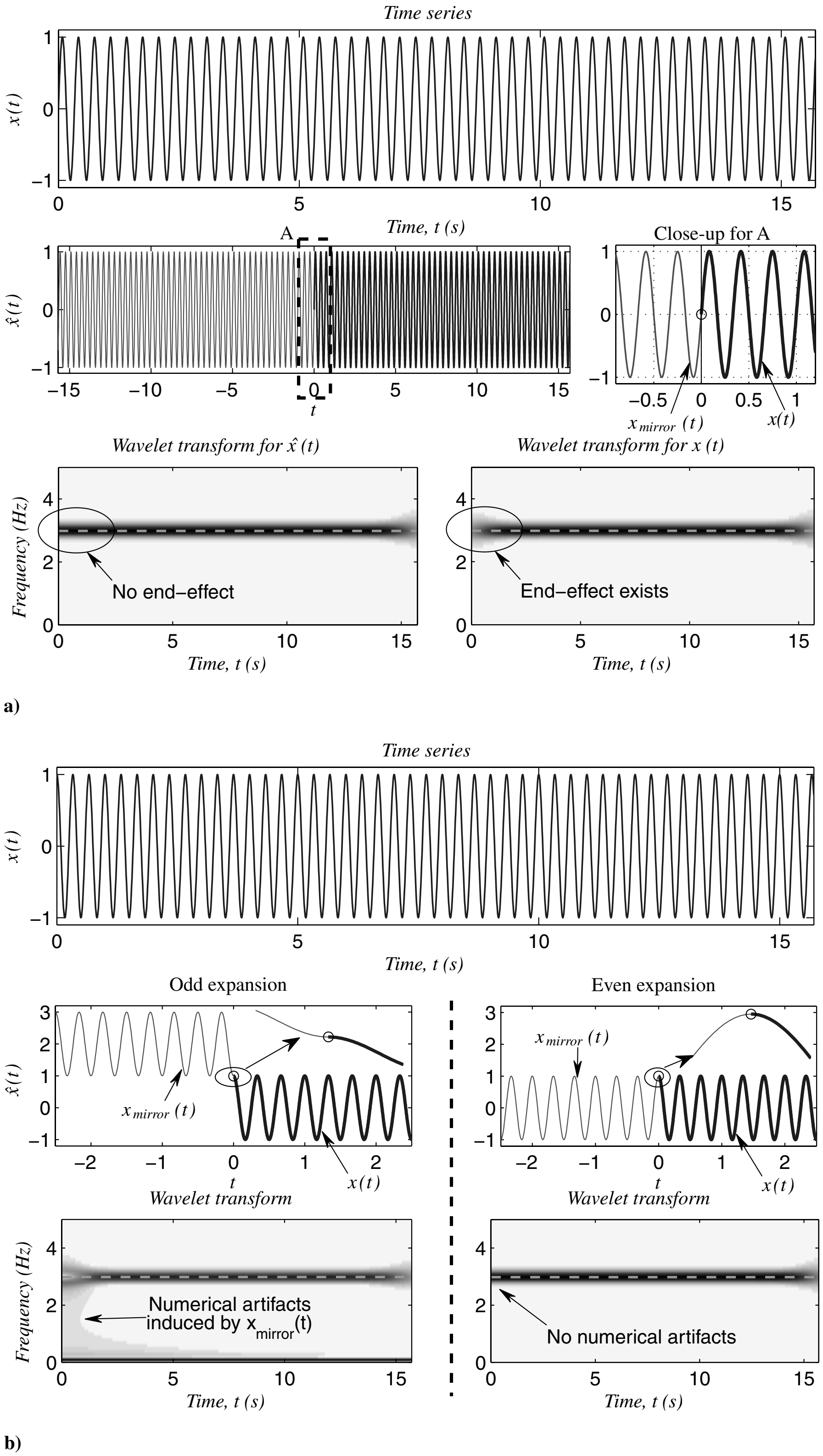

Fig. 3 Time-frequency analysis of $x(t)$ expanded with a mirror-image signal: a) $x(t) = \sin(2\pi f_1 t), f_1 = 3$ (Hz); and b) $x(t) = \cos(2\pi f_1 t), f_1 = 3$ (Hz).

We also note that to perform EMD analysis of a time series suspected to contain hidden high-frequency components as in Fig. 4a, one may (numerically) differentiate with respect to time to magnify such hidden high-frequency contents (and filter to remove the additional high-frequency noise induced by the numerical differentiation). Thus, for the previous example we obtain $\dot{x}(t) = -2\pi f_1 \sin(2\pi f_1 t) - 0.6\pi f_2 \sin(2\pi f_2 t)$, where the amplitude of the f_2-component becomes multiplied by the factor of $2\pi f_2$, as depicted in Fig. 6a. In this case one does not even need to use a masking signal to separate the two frequency components because the amplitudes of the respective components become of compatible orders in the differentiated signal: the component at frequency $2\pi f_1$ is equal to 6.282, whereas the amplitude of the component at frequency $0.6\pi f_2$ is equal to 5.655. Figure 6b presents the two components of the previous example with the help of the masking signal $x_{\text{mask}}(t) = -0.5 x_{\max} \sin(2\pi \bar{f} t)$, where in this case the masking frequency $\bar{f} = f_2$ is tuned to the highest component of the time series. Because the influence of the masking signal is eliminated when the pair of

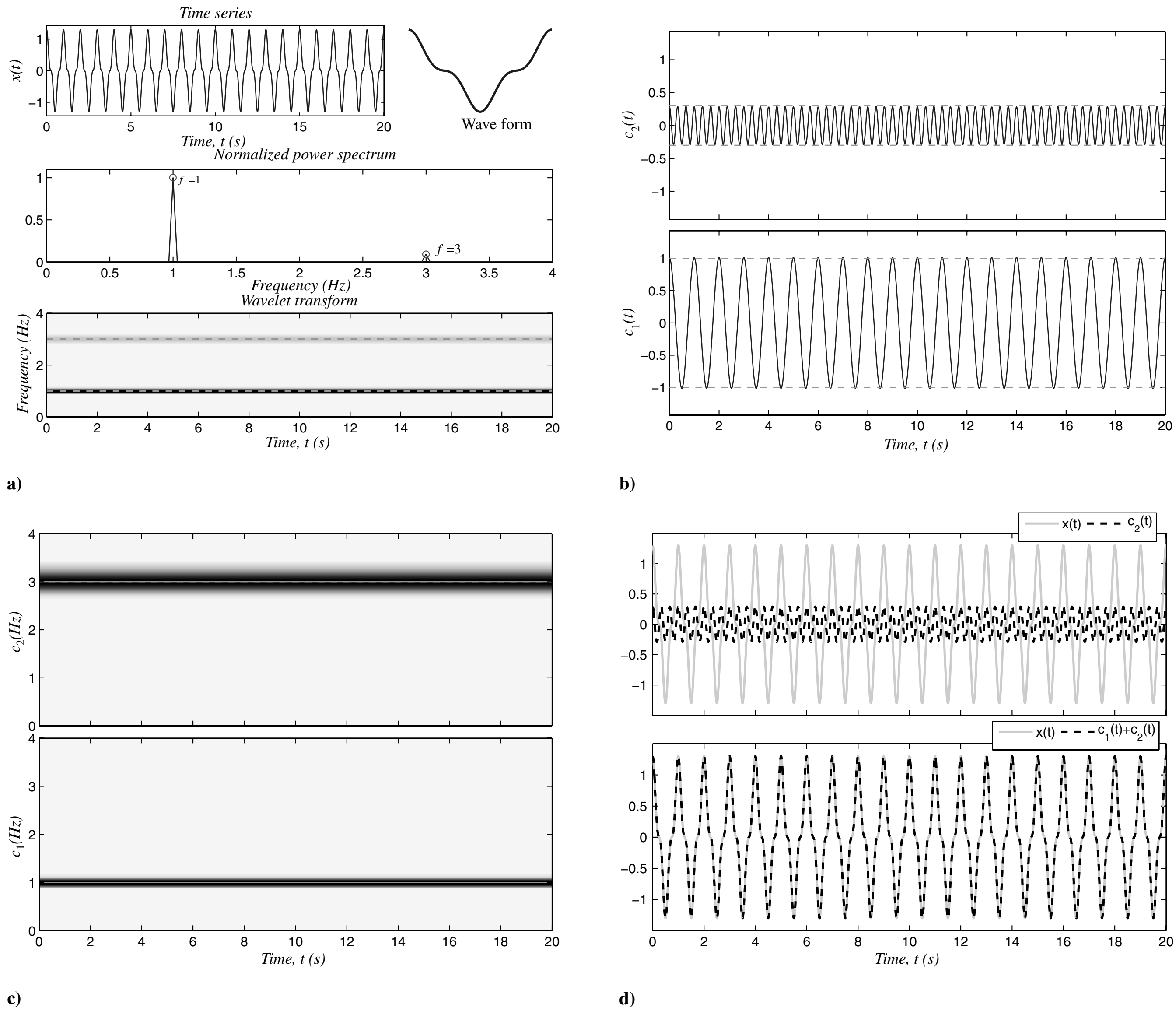

Fig. 4 EMD analysis for $x(t) = \cos(2\pi f_1 t) + 0.3\cos(2\pi f_2 t)$, where $f_1 = 1$ and $f_2 = 3$ (Hz), when the masking signal $x_{\mathrm{mask}}(t) = 0.5x_{\max}\cos(2\pi\bar{f}t)$, $\bar{f} = f_1 + f_2$, is applied: a) time series, power spectrum and wavelet transform spectra; b) dominant IMFs; c) instantaneous frequencies in wavelet transform spectra; and d) reconstruction of the signal (index of orthogonality: 1.65×10^{-3}).

positive and negative IMFs are averaged, the first IMF will recover the original highest-frequency content of the time series. The instantaneous frequencies of the resulting two IMFs are depicted in Fig. 6c, whereas their completeness, i.e., their capacity to reproduce the original signal by superposition, is demonstrated in Fig. 6d.

IV. Correspondence Between Analytical and Empirical Slow Flows

Once proper (monocomponent or narrowband) IMFs are obtained by EMD or AEMD, the Hilbert transformation can be applied to them. Let $u(t)$ be the original (real) signal. Then, its Hilbert transform $v(t)$ is defined by the integral

$$v(t) = \mathcal{H}[u(t)] \triangleq \frac{\mathrm{PV}}{\pi}\int_{-\infty}^{\infty}\frac{u(s)}{t-s}\mathrm{d}s \tag{12}$$

where $\mathcal{H}[\cdot]$ and PV imply Hilbert transformation and the Cauchy principal value of the integral, respectively. The inverse Hilbert transformation is defined by the formula:

$$u(t) = \mathcal{H}^{-1}[v(t)] \triangleq \frac{\mathrm{PV}}{\pi}\int_{-\infty}^{\infty}\frac{v(s)}{s-t}\mathrm{d}s \tag{13}$$

In convolution notation, the Hilbert pair $\{u(t), v(t)\}$ can be written as

$$v(t) = u(t) * \frac{1}{\pi t}, \qquad u(t) = v(t) * \frac{1}{\pi t} \tag{14}$$

Note that unlike other transformations the Hilbert transformation does not change the domain of the signal.

Recalling that the Fourier pair $\{\, u(t), \quad U(\omega)\,\}$ is expressed as

$$\begin{aligned} U(\omega) &= \mathcal{F}[u(t)] \triangleq \int_{-\infty}^{\infty} u(t)e^{-j\omega t}\mathrm{d}t \\ u(t) &= \mathcal{F}^{-1}[U(\omega)] \triangleq \int_{-\infty}^{\infty} U(\omega)e^{j\omega t}\mathrm{d}f \end{aligned} \tag{15}$$

where $\omega = 2\pi f$, we can compose the following diagram relating the Fourier and Hilbert transforms.

$$\begin{tikzcd} u(t) \arrow[r, mapsto, "\mathcal{H}"] \arrow[d, "\mathcal{F}"'] & v(t) \arrow[d, "\mathcal{F}"] \\ U(\omega) \arrow[r, mapsto, "\mathcal{H}"] & V(\omega) \end{tikzcd} \tag{16}$$

Noting that the Fourier transform of the kernel of the Hilbert transform, $1/(\pi t)$, is $-j\mathrm{sgn}(\omega)$, one can derive the relation

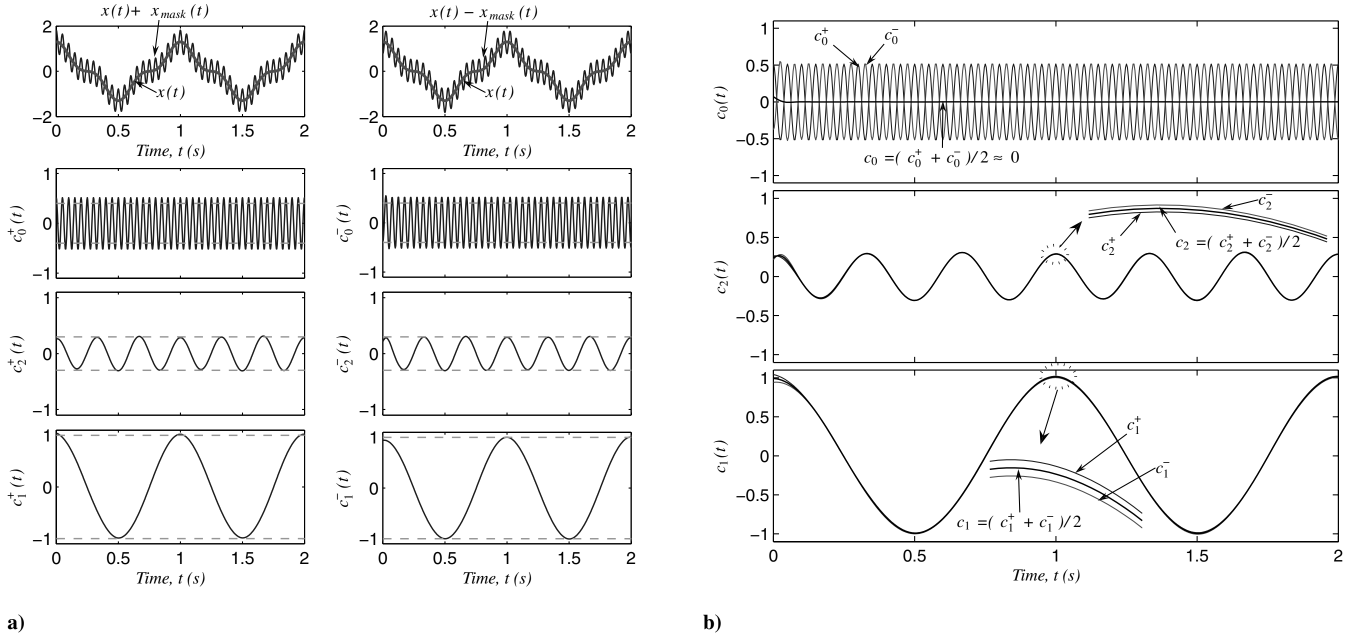

Fig. 5 Schematic of how a masking signal $x_{\text{mask}}(t) = 0.4x_{\max}\cos(2\pi\bar{f}t), \bar{f} = 20f_1$ is applied for the time series of Fig. 4a: a) the EMD analysis for $x(t) \pm x_{\text{mask}}(t)$; and b) resulting IMFs (index of orthogonality: 4.7 x 10^{-3}).

$$v(t) \overset{\mathcal{F}}{\mapsto} V(\omega) = -j\,\mathrm{sgn}(\omega)U(\omega) \tag{17}$$

where $U(\omega)$ and $V(\omega)$ form a Hilbert pair, and the spectrum of $u(t)$ is multiplied by the operator $-j\,\mathrm{sgn}(\omega)$. It is interesting to note that the Hilbert transform can be calculated by the Fourier transform and inverse Fourier transform:

$$u(t) \overset{\mathcal{F}}{\mapsto} U(\omega) \overset{\mathcal{H}}{\mapsto} V(\omega) = -j\,\mathrm{sgn}(\omega)U(\omega) \overset{\mathcal{F}^{-1}}{\mapsto} v(t) \tag{18}$$

It is well known that the complex signal whose imaginary part is the Hilbert transform of its real part is an analytic signal. A simple example is the harmonic complex signal,

$$\psi(t) = \exp(j\omega t) = \cos(\omega t) + j\sin(\omega t) \equiv \cos(\omega t) + j\mathcal{H}[\cos(\omega t)]$$

Moreover, we recall that, by the Cauchy–Riemann theorem, the function $\psi(z) = u(x, y) + jv(x, y)$ is called analytic in the domain $D \subset \mathbb{C}$, $z = x + jy \in D$ if and only if the real functions $u(x, y)$ and $v(x, y)$ are continuously differentiable (i.e., C^1).

Consider an analytic signal

$$\psi(t) = u(t) + jv(t) = A(t)e^{j\theta(t)} \tag{19}$$

where the real signals $u(t)$ and $v(t)$ are the Hilbert pair defined in Eq. (14). Then, $u(t)$ and $v(t)$ can be written in terms of analytic signals,

$$u(t) = \frac{\psi(t) + \psi^*(t)}{2}, \qquad v(t) = \frac{\psi(t) - \psi^*(t)}{2j} \tag{20}$$

where $\psi^*(t) = u(t) - jv(t)$ is the conjugate analytic signal. Equations (19) and (20) will provide the insight necessary to explain equivalence between analytical and empirical slow flows.

For the analytic signal (19), the instantaneous amplitude envelope $A(t)$ and phase $\theta(t)$ of the complex signal $\psi(t)$ can be computed by the expressions

$$A(t) = \sqrt{u(t)^2 + v(t)^2}, \qquad \theta(t) = \tan^{-1}\frac{v(t)}{u(t)} \tag{21}$$

which yield the instantaneous frequency of the signal by differentiation.

$$\omega(t) = \frac{d\theta}{dt} = \frac{d}{dt}\left[\tan^{-1}\frac{v(t)}{u(t)}\right] = \frac{u(t)\dot{v}(t) - v(t)\dot{u}(t)}{u^2(t) + v^2(t)} \tag{22}$$

Although Eq. (22) defines the instantaneous frequency of a signal regardless of its bandwidth, it has been observed that the notion of instantaneous frequency has physical meaning only for narrowband signals (i.e., high-frequency modulated signals [9]). It is possible, however, to implement frequency demodulation for wideband signals such as speech by regarding the instantaneous frequency as the average of all frequencies that exist at a given instant, and the instantaneous bandwidth can be considered as the frequency deviation from that average [37].

Extending the fundamentals of an analytic signal, we examine the analyticity aspects of IMFs [37] to establish correspondence or equivalence between an (analytical) slow-flow model defined by the CX-A technique and the dominant (proper) IMFs (i.e., the empirical slow-flow) resulting from EMD analysis. As mentioned previously, EMD analysis is an iterative process that decomposes a real signal $x_k(t)$ (which represents the response of the kth DOF of an n-DOF dynamical system) into a set of IMFs, as expressed by Eq. (8),

$$x_k(t) \approx c_1^{(k)}(t) + c_2^{(k)}(t) + \cdots + c_N^{(k)}(t), \qquad k = 1, 2, \ldots, n \tag{23}$$

where $c_m^{(k)}(t)$, $m = 1, 2, \ldots, N$, is the mth component, associated with frequency ω_m.

Motivated by the previous discussion of analytic complex signals, we introduce the following complexification of the mth IMF, $c_m^{(k)}(t)$,

$$\hat{\psi}_k^{(m)}(t) = c_m^{(k)}(t) + j\mathcal{H}[c_m^{(k)}(t)] \triangleq \hat{A}_m^{(k)}(t)e^{j\hat{\theta}_m^{(k)}(t)} \tag{24}$$

which by construction is an analytic signal. The instantaneous envelope and phase of this IMF can then be computed similarly to Eq. (21),

$$\hat{A}_m^{(k)}(t) = \sqrt{c_m^{(k)}(t)^2 + \mathcal{H}[c_m^{(k)}(t)]^2}, \qquad \hat{\theta}_m^{(k)}(t) = \tan^{-1}\left[\frac{\mathcal{H}[c_m^{(k)}(t)]}{c_m^{(k)}(t)}\right] \tag{25}$$

and its instantaneous frequency, similarly to Eq. (22),

$$\hat{\omega}_m^{(k)}(t) = \frac{d}{dt}\hat{\theta}_m^{(k)}(t) = \frac{c_m^{(k)}(t)\frac{d}{dt}\mathcal{H}[c_m^{(k)}(t)] - \dot{c}_m^{(k)}(t)\mathcal{H}[c_m^{(k)}(t)]}{c_m^{(k)}(t)^2 + \mathcal{H}[c_m^{(k)}(t)]^2} \tag{26}$$

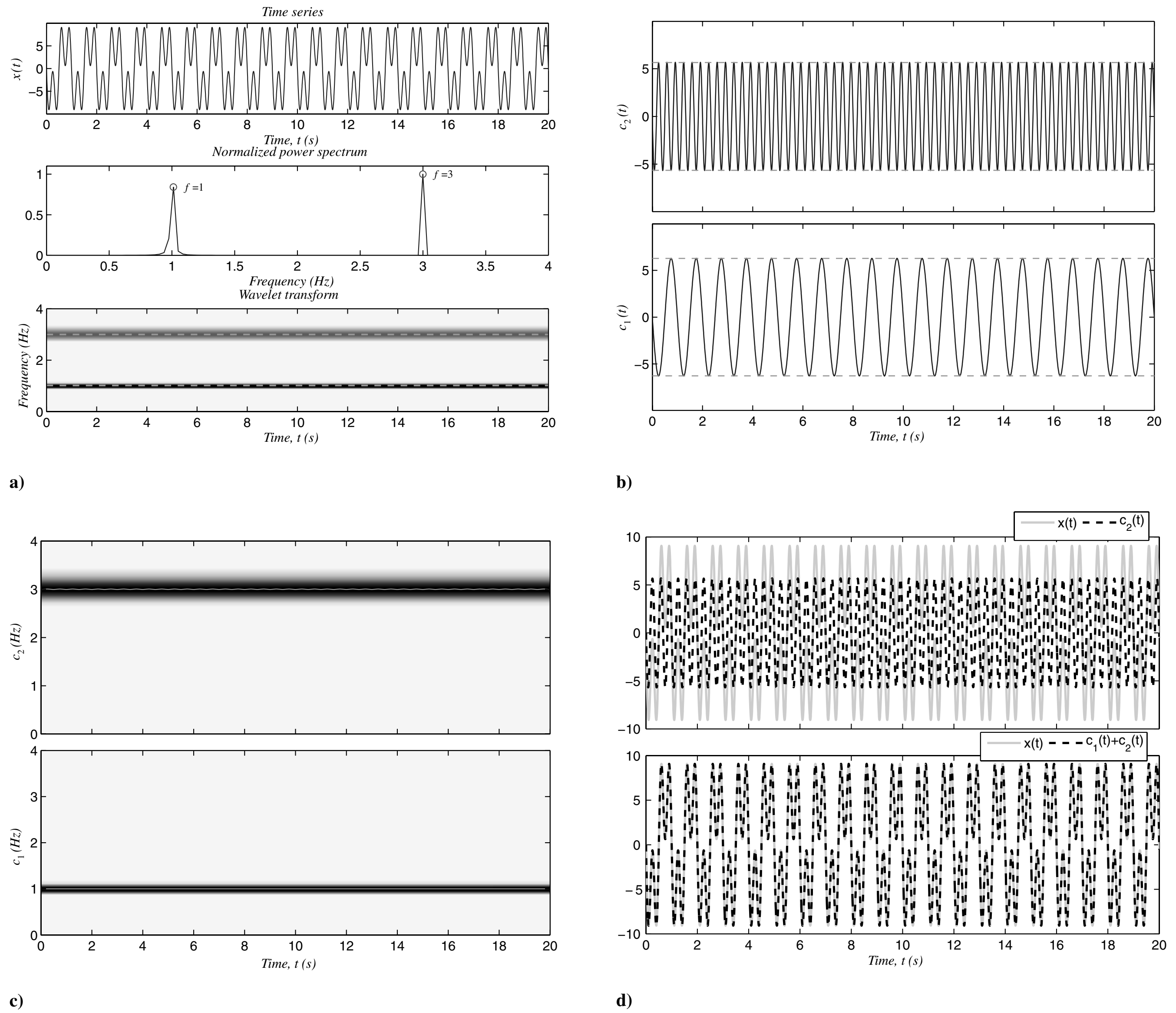

Fig. 6 **EMD analysis for $x(t) = -2\pi f_1 \sin(2\pi f_1 t) - 0.6\pi f_2 \sin(2\pi f_2 t)$, i.e., the derivative of the time series in Fig. 4a, when the masking signal $x_{\text{mask}}(t) = -0.5 x_{\max} \sin(2\pi \bar{f} t), \bar{f} = f_2$ is applied: a) time series, power spectrum, and wavelet transform spectra; b) dominant IMFs; c) instantaneous frequencies in wavelet transform spectra; and d) reconstruction of the signal (index of orthogonality: 2.68 × 10^{-3}).**

It follows that the analytic signal (24) can be partitioned in terms of slow and fast components according to the expression

$$\hat{\psi}_k^{(m)}(t) = \hat{A}_m^{(k)}(t) e^{j[\hat{\theta}_m^{(k)}(t) - \omega_m t]} e^{j\omega_m t} \tag{27}$$

which is in a form similar to the analytical slow flow of Eq. (5), although no a priori slow–fast partition of the dynamics was assumed when decomposing the IMF. Recognizing $e^{j\omega_m t}$ as the fast dynamics of the IMF, we conclude that the remaining partition $\hat{A}_m^{(k)}(t) e^{j[\hat{\theta}_m^{(k)}(t) - \omega_m t]}$ plays the role of the slow dynamics. Clearly, for such a slow–fast partition of the IMF to hold it must be satisfied that the instantaneous amplitude, phase, and frequency of the IMF are slowly varying compared with the corresponding fast-frequency ω_m of the IMF. This is an assumption that will be made throughout this study, in order for the results of EMD to conform with the following theoretical developments.

Now, we consider an alternative complexification of the mth IMF $c_m^{(k)}(t)$ in the form,

$$\hat{\hat{\psi}}_k^{(m)}(t) = \dot{c}_m^{(k)}(t) + j\omega_m c_m^{(k)}(t) \triangleq \hat{\hat{A}}_m^{(k)}(t) e^{j\hat{\hat{\theta}}_m^{(k)}(t)} \tag{28}$$

which bears similarity to the complexification (5). If the complex function $\hat{\hat{\psi}}_k^{(m)}(t)$ is analytic, then so is the function $j\hat{\hat{\psi}}_k^{(m)}(t) = -\omega_m c_m^{(k)}(t) + j\dot{c}_m^{(k)}(t)$. This implies that its imaginary part is the Hilbert transform of its real part,

$$\dot{c}_m^{(k)}(t) = -\omega_m \mathcal{H}[c_m^{(k)}(t)] \tag{29}$$

Furthermore, if the condition (29) is satisfied, then there should be an equivalence between the analytical slow flow defined by Eq. (4) and the analytical empirical slow flow defined by Eq. (8). This is because both expressions represent identical analytical decompositions of the time series in terms of slowly modulated components at distinct fast frequencies. It follows that the following expressions should hold

$$x_k^{(m)}(t) \equiv c_m^{(k)}(t) \quad \text{and} \quad \dot{x}_k^{(m)}(t) \equiv \dot{c}_m^{(k)}(t) \tag{30}$$

which imply that $\dot{c}_m^{(k)}(t)$ is identical to the mth IMF of the velocity signal $\dot{x}_k^{(m)}(t)$. Then, Eq. (28) can be rewritten as

$$\begin{aligned} \hat{\hat{\psi}}_k^{(m)}(t) &= \dot{c}_m^{(k)}(t) + j\omega_m c_m^{(k)}(t) = -\omega_m \mathcal{H}[c_m^{(k)}(t)] + j\omega_m c_m^{(k)}(t) \\ &= j\omega_m (c_m^{(k)}(t) + j\mathcal{H}[c_m^{(k)}(t)]) = j\omega_m \hat{\psi}_k^{(m)}(t) \end{aligned} \tag{31}$$

Therefore, the analytic signal $\hat{\psi}_k^{(m)}(t)$ in Eq. (24) and the complex function $\hat{\hat{\psi}}_k^{(m)}(t)$ [which is also analytic by Eq. (29)] in Eq. (28) are equivalent, such that

$$\hat{\psi}_k^{(m)}(t) = \frac{1}{j\omega_m}\hat{\hat{\psi}}_k^{(m)}(t) \equiv \frac{1}{j\omega_m}\psi_k^{(m)}(t) \qquad (32)$$

where $\psi_k^{(m)}(t)$ is derived from a mathematical (or analytical) model by the (analytic) complexification in Eq. (5), whereas $\hat{\hat{\psi}}_k^{(m)}(t)$ is obtained by the EMD (or AEMD) of the (experimental or numerical) measured time series via Eq. (8) and its complexification (28).

Now, we can conclude the correspondence between the analytical and empirical slow flows by noting that Eq. (32) leads to the following equivalence of the slow parts resulting from analysis and EMD,

$$\hat{A}_m^{(k)}(t)e^{j[\hat{\theta}_m^{(k)}(t)-\omega_m t]} \approx \frac{1}{j\omega_m}\varphi_k^{(m)}(t) \qquad (33)$$

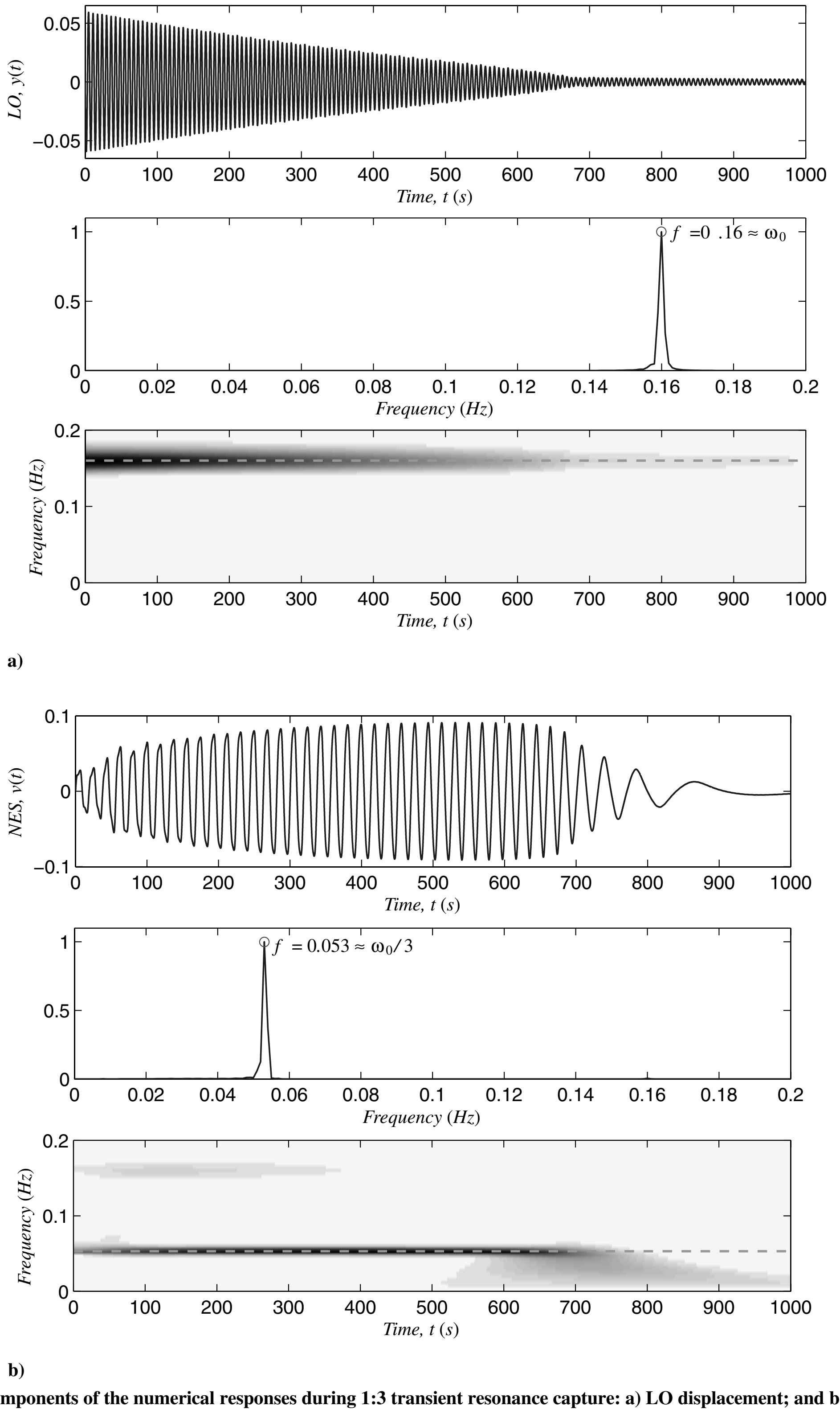

Fig. 7 Frequency components of the numerical responses during 1:3 transient resonance capture: a) LO displacement; and b) NES displacement.

from which the analytical slow flow can be expressed in terms of the empirical slow flow as follows:

$$\varphi_k^{(m)}(t) \approx j\omega_m \hat{A}_m^{(k)}(t) e^{j[\hat{\theta}_m^{(k)}(t)-\omega_m t]} \tag{34}$$

The equivalence between the analytical and empirical slow flows based on the assumption of analyticity of the IMFs can be restated as follows. From Eqs. (5), (6), and (30), we write

$$\begin{aligned}\hat{\psi}_k^{(m)}(t) &= \dot{c}_m^{(k)}(t) + j\omega_m c_m^{(k)}(t)\\ &\equiv \psi_k^{(m)}(t) = \varphi_k^{(m)}(\tau)e^{j\omega_m t}\\ &= |\varphi_k^{(m)}(\tau)|e^{j\theta_k^{(m)}(\tau)}e^{j\omega_m t}\\ &= |\varphi_k^{(m)}(\tau)|e^{j[\omega_m t+\theta_k^{(m)}(\tau)]}\end{aligned} \tag{35}$$

where the slow-time scale τ is introduced to indicate that the complex variable $\varphi_k^{(m)}(\tau)$ is a slowly varying component with respect to the

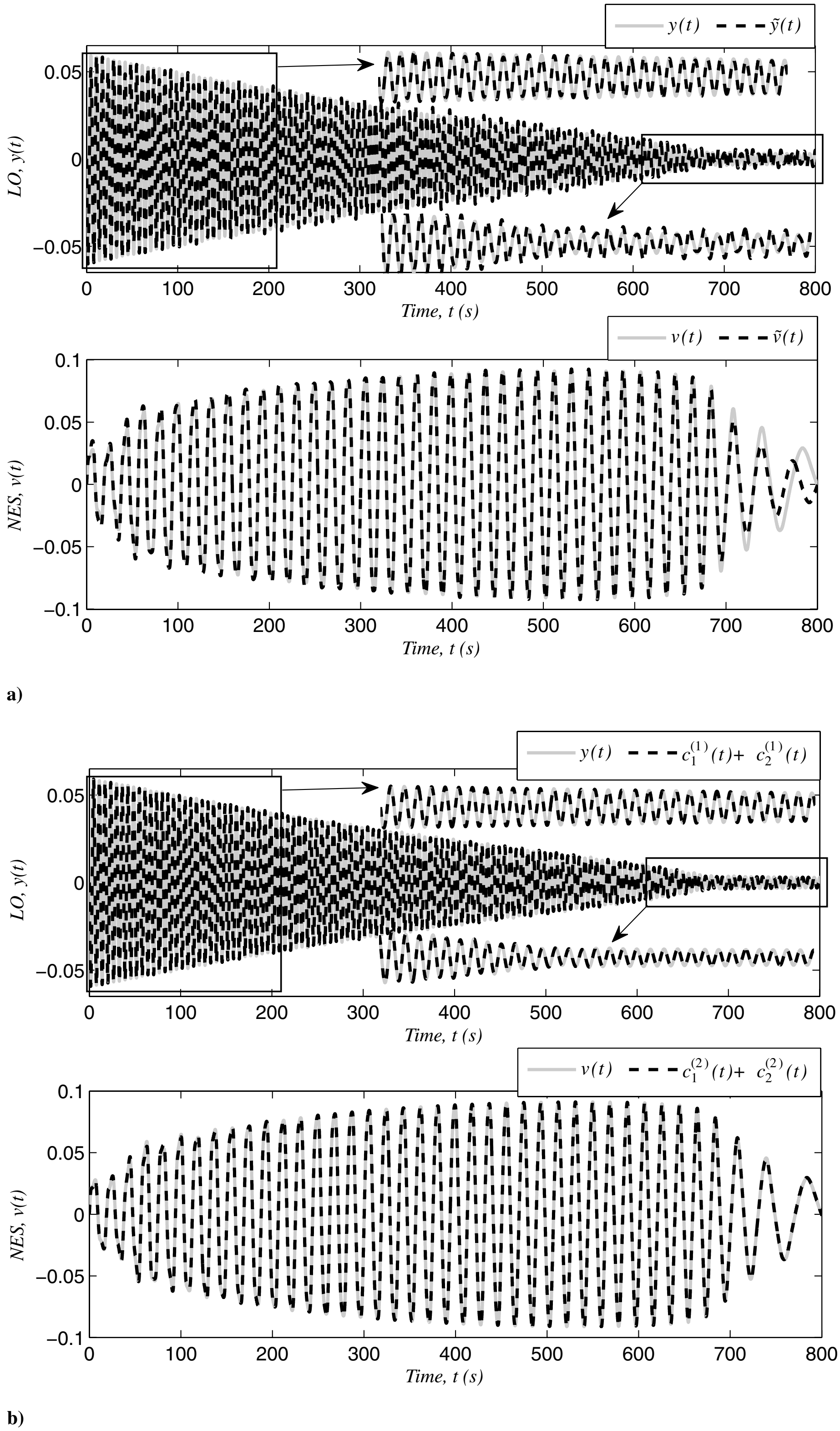

Fig. 8 Comparison of exact responses and corresponding approximations resulting from a) analysis (CX-A); and b) AEMD.

fast-varying part $e^{j\omega_m t}$. In this multiscale formulation the slow temporal variable τ is considered to be independent from the fast temporal variable t [31]. Thus, the slowly varying envelope and phase, $|\varphi_k^{(m)}(\tau)|$ and $\theta_k^{(m)}(\tau)$, are equivalent to the corresponding quantities, $\omega_m \hat{A}_m^{(k)}(t)$ and $\hat{\theta}_m^{(k)}(t) - \omega_m t$, in Eq. (34), respectively.

The empirical slow flow can then be expressed in terms of the real and imaginary parts of $\psi_k^{(m)}(t)$ such that

$$c_m^{(k)}(t) = \frac{1}{\omega_m}\mathrm{Im}[\varphi_k^{(m)}(\tau)e^{j\omega_m t}] = \frac{1}{\omega_m}|\varphi_k^{(m)}(\tau)|\sin[\omega_m t + \theta_k^{(m)}(\tau)]$$
$$\dot{c}_m^{(k)}(t) = Re[\varphi_k^{(m)}(\tau)e^{j\omega_m t}] = |\varphi_k^{(m)}(\tau)|\cos[\omega_m t + \theta_k^{(m)}(\tau)] \tag{36}$$

Recalling that $\mathcal{H}[\cos\omega t] = \sin\omega t$ and $\mathcal{H}[\sin\omega t] = -\cos\omega t$, we derive

$$\begin{aligned}\mathcal{H}[c_m^{(k)}(t)] &= \frac{1}{\omega_m}\mathcal{H}[|\varphi_k^{(m)}(\tau)|\sin[\omega_m t + \theta_k^{(m)}(\tau)]] \\ &= \frac{1}{\omega_m}|\varphi_k^{(m)}(\tau)|\mathcal{H}[\sin[\omega_m t + \theta_k^{(m)}(\tau)]] \\ &= -\frac{1}{\omega_m}|\varphi_k^{(m)}(\tau)|\cos[\omega_m t + \theta_k^{(m)}(\tau)] \\ &= -\frac{1}{\omega_m}|\varphi_k^{(m)}(\tau)|\cos[\omega_m t + \theta_k^{(m)}(\tau)] = -\frac{1}{\omega_m}\dot{c}_m^{(k)}(t)\end{aligned} \tag{37}$$

where Hilbert transformation is carried out only with respect to the fast time scale. This verifies the condition (29) for the analytic equivalence between the slow-flow and dominant IMFs. But even without introducing the slow time scale in Eq. (35), one can derive the analyticity condition (37) by means of the Bedrosian theorem [42] based on the analyticity of the slow flow $\varphi_k^{(m)}(t)$ with the notation of the fast time scale retained.

Again, we emphasize that we applied the Hilbert transformation only with respect to the fast time scale in Eq. (37), ignoring the slow-time dependence. That is, if a function behaves as a simple harmonic function, $c(t) = Ae^{j\omega t}$ (A constant with respect to time variation), then $\dot{c}(t) = j\omega Ae^{j\omega t} = j\omega c(t)$. Hilbert transformation of the harmonic function yields $\mathcal{H}[c(t)] = -je^{j\omega t} = -jc(t)$ so that $\mathcal{H}\{[\mathcal{H}[c(t)]\} = -c(t)$. This leads to the relations $\dot{c}(t) = -\omega\mathcal{H}[c(t)]$ and $\ddot{c}(t) = -\omega^2 c(t) \Rightarrow \ddot{c}(t) + \omega^2 c(t) = 0$. This last expression obviously represents a harmonic oscillator, and can be applied to proper IMFs. That is, we write

$$\ddot{c}_m^{(k)}(t) + \omega_m^2 c_m^{(k)}(t) = 0 \tag{38}$$

which indicates that the assumed slow–fast partition of the IMFs and the assumption of harmonic dependence with respect to the fast time scale imply the analyticity condition (29) for these IMFs.

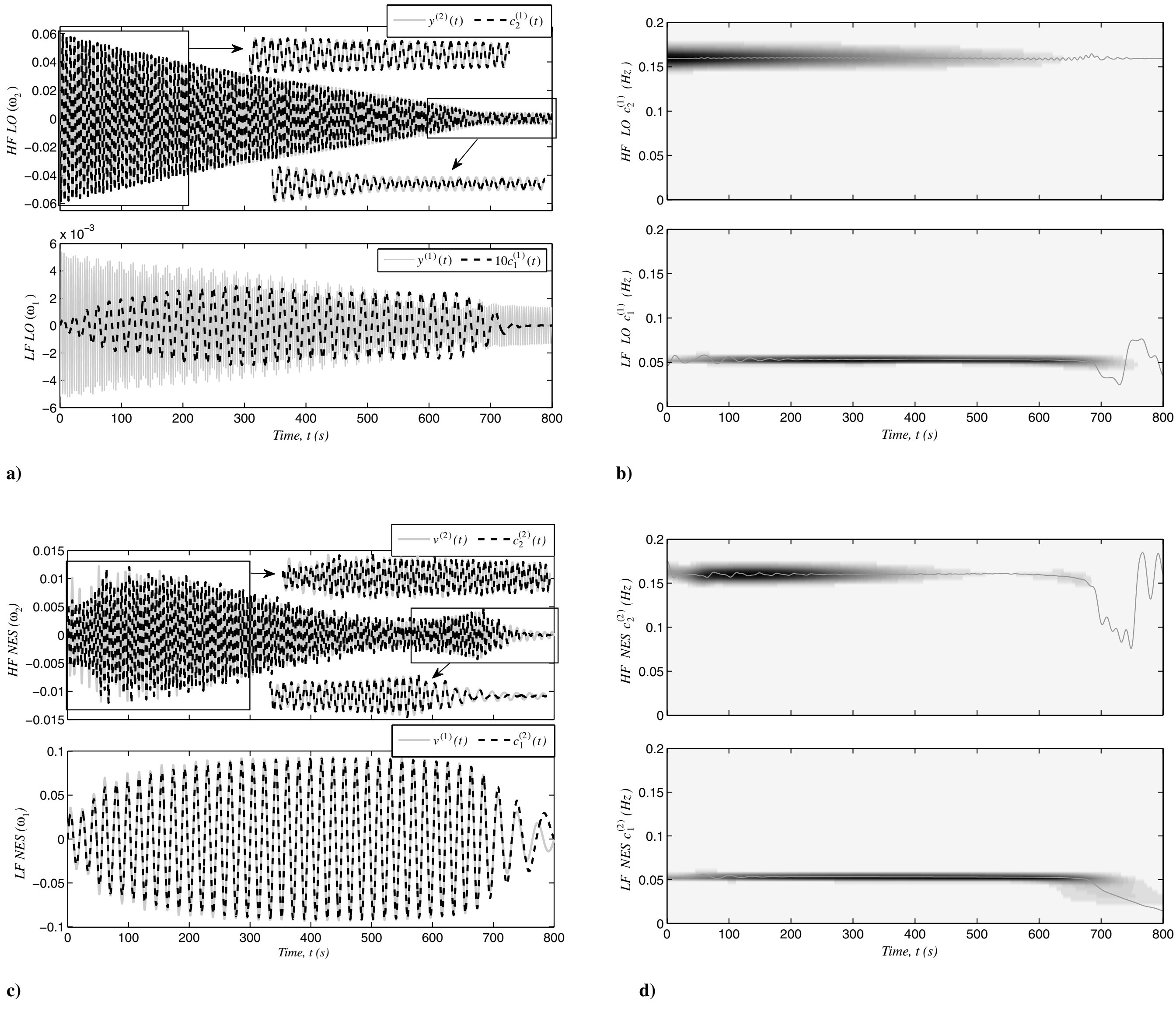

a) b) c) d)

Fig. 9 Comparison of respective frequency components of displacements derived from the analytical slow flow and the IMFs (parts a and c); the wavelet spectra of the IMFs (parts b and d, respectively); the instantaneous frequencies of the IMFs are superimposed on the wavelet spectra.

Finally, the analytic condition for slow flow leads to an interesting conclusion regarding the instantaneous frequency in Eq. (26). Evaluate the numerator of the instantaneous frequency of the IMF to obtain the relation

$$c_m^{(k)}(t)\frac{d}{dt}\mathcal{H}[c_m^{(k)}(t)] - \dot{c}_m^{(k)}(t)\mathcal{H}[c_m^{(k)}(t)] = c_m^{(k)}(t)[\omega_m c_m^{(k)}(t)] - \{-\omega_m \mathcal{H}[c_m^{(k)}(t)]\}\mathcal{H}[c_m^{(k)}(t)] = \omega_m[c_m^{(k)}(t)^2 + \mathcal{H}[c_m^{(k)}(t)]^2] \qquad (39)$$

This implies that, for a proper IMF, the instantaneous (fast) frequency calculated by Eq. (26) is ω_m on average. In other words, the slow phase becomes a constant on average. We remark that if the slow amplitude varies significantly in the fast time scale, this relation does not expect to hold.

The derivations in this section show that we can associate the EMD results to the underlying slow-flow dynamics, a result that provides a physics-based foundation for EMD. In particular, we showed that if

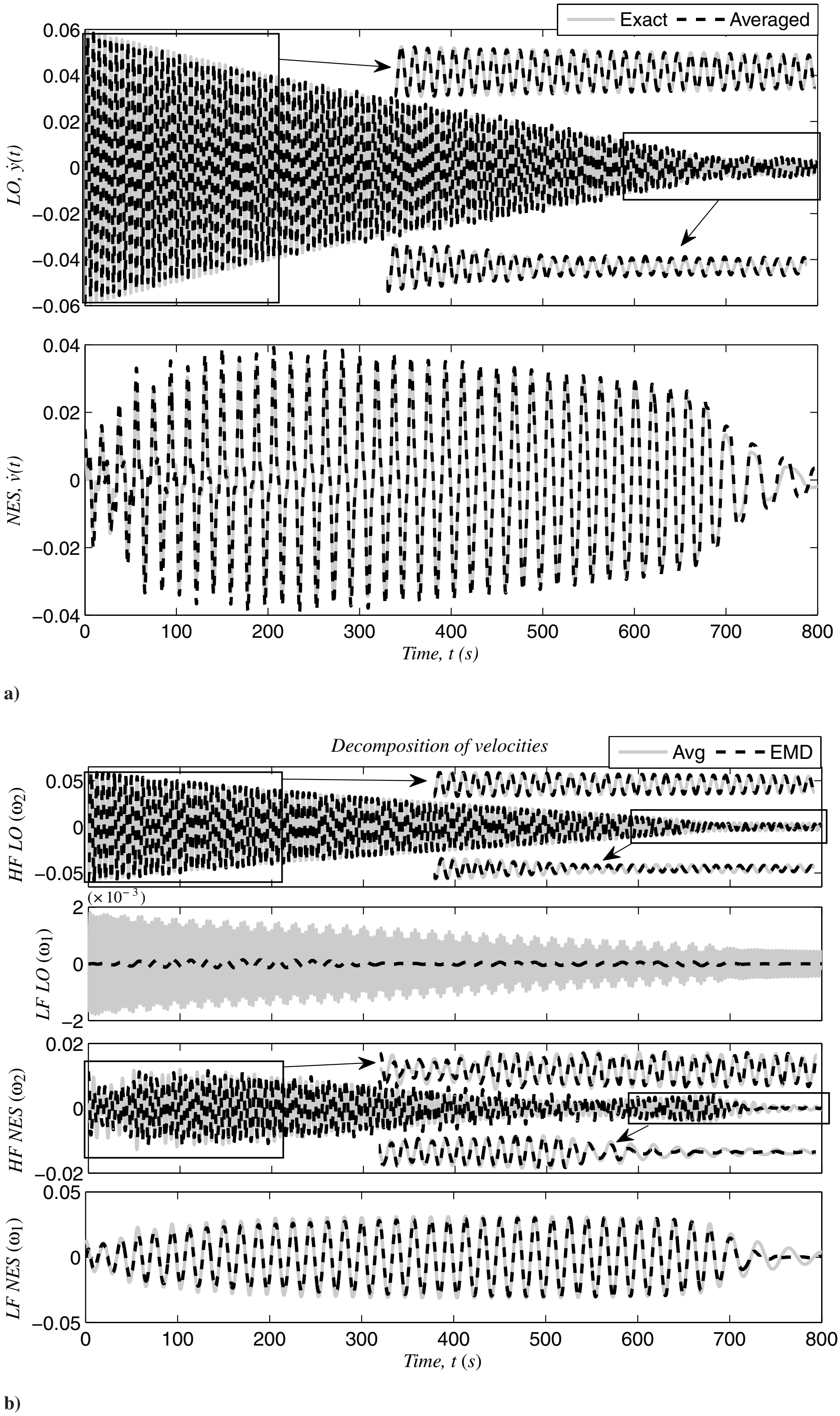

Fig. 10 Decomposition of velocities: comparison of a) the exact responses with approximate responses derived from the analytical slow flow; and b) the respective components from the analytical and empirical slow flows.

the analyticity condition (29) is satisfied then proper IMFs can be associated with components of the slow dynamics of corresponding frequencies. In summary, by associating the EMD results to the slow-flow dynamics of a dynamical system we demonstrate that the IMFs provide significant physical insight to the dynamics, a feature that will be employed by the authors in a companion paper for nonlinear system identification and reduced-order modeling [30]. In the following section we provide some demonstrative examples that highlight the correspondence between EMD results and slow flows.

V. Examples of Applications

In this section, we demonstrate the correspondence between the analytical and empirical slow flows established in Sec. IV based on the analyticity of IMFs. The dynamical processes considered are 1) the dynamics of 1:3 transient resonance capture in a coupled oscillator [35]; and 2) the triggering mechanism of aeroelastic instability in a rigid wing in flow [36]. For both systems, the analytical slow-flow models are already developed in previous works, and so a direct study of their equivalence to IMFs derived from AEMD is possible.

A. Dynamics of 1:3 Transient Resonance Capture in a Coupled Oscillator

We consider first a linear oscillator (LO) coupled to a nonlinear oscillator by means of an essential stiffness nonlinearity of the third degree. In previous works the nonlinear oscillator was termed a nonlinear energy sink (NES) due to its capacity to passively absorb and locally dissipate energy from the LO over broad frequency ranges [32]. The equations of motion of this system are

$$\begin{aligned}&\ddot{y}+\omega_0^2 y+\epsilon\lambda_1\dot{y}+\epsilon\lambda_2(\dot{y}-\dot{v})+C(y-v)^3=0\\&\epsilon\ddot{v}+\epsilon\lambda_2(\dot{v}-\dot{y})+C(v-y)^3=0\end{aligned}\tag{40}$$

where y and v are the displacements of the LO and NES, respectively; ω_0 is the linearized natural frequency of the LO; ϵ the mass ratio of the NES to the LO; C the essentially nonlinear stiffness coefficient; and $\lambda_{1,2}$ the damping coefficients. In the application studied we consider the parameters $\omega_0 = 1$, $C = 1$, $\epsilon = 0.05$, and $\lambda_{1,2} = 0.03$, so that $\epsilon\lambda_{1,2} = 0.0015$. The initial conditions $\dot{y}(0) = -0.059443193$ and $\dot{v}(0) = 0.014995493$ with zero initial displacements initiate transient responses corresponding to 1:3 transient resonance capture between the LO and the NES; i.e., transient nonlinear resonance between the linear and nonlinear oscillators, with the linear oscillator oscillating three times faster than the nonlinear one. Strong energy exchanges between the two oscillators occur during this resonance capture [34,35].

Figure 7 depicts the corresponding responses in the time and frequency domains. From these responses, we infer that the dominant frequencies for the LO and NES are $\omega_2 = \omega_0$ (high-frequency component, denoted by HF) and $\omega_1 = \omega_0/3$ (low-frequency component, denoted by LF), respectively. Kerschen et al. [35] showed that during the engagement of the 1:3 transient resonance capture (approximately until $t = 650$), the LO and NES behave as a system of two uncoupled harmonic oscillators with fundamental frequencies equal to ω_0 and $\omega_0/3$, respectively, which is evidenced by the constant time-frequency behavior in the wavelet transform spectra. In reality, the two oscillators possess both ω_1 and ω_2 harmonic components due to nonlinear modal interactions.

To derive an analytical slow-flow model for the 1:3 transient resonance capture, we assume that each of the two responses of the system can be decomposed into two frequency components,

$$\begin{aligned}x_1(t)&\triangleq y(t)=y^{(1)}(t)+y^{(2)}(t)\\x_2(t)&\triangleq v(t)=v^{(1)}(t)+v^{(2)}(t)\end{aligned}\tag{41}$$

where subscripts denote the DOF, and superscripts refer to the dependence on the frequency components, ω_1 and ω_2, respectively. According to the CX-A technique we introduce the following complex variables (i.e., complexify the real variables)

$$\begin{aligned}\psi_1^{(1)}(t)&=\dot{y}^{(1)}(t)+j\omega_1 y^{(1)}(t)\equiv\varphi_1^{(1)}(t)e^{j\omega_1 t}\\\psi_1^{(2)}(t)&=\dot{y}^{(2)}(t)+j\omega_2 y^{(2)}(t)\equiv\varphi_1^{(2)}(t)e^{j\omega_2 t}\\\psi_2^{(1)}(t)&=\dot{v}^{(1)}(t)+j\omega_1 v^{(1)}(t)\equiv\varphi_2^{(1)}(t)e^{j\omega_1 t}\\\psi_2^{(2)}(t)&=\dot{v}^{(2)}(t)+j\omega_2 v^{(2)}(t)\equiv\varphi_2^{(2)}(t)e^{j\omega_2 t}\end{aligned}\tag{42}$$

so the real displacements and velocities can be expressed in terms of the new complex variables,

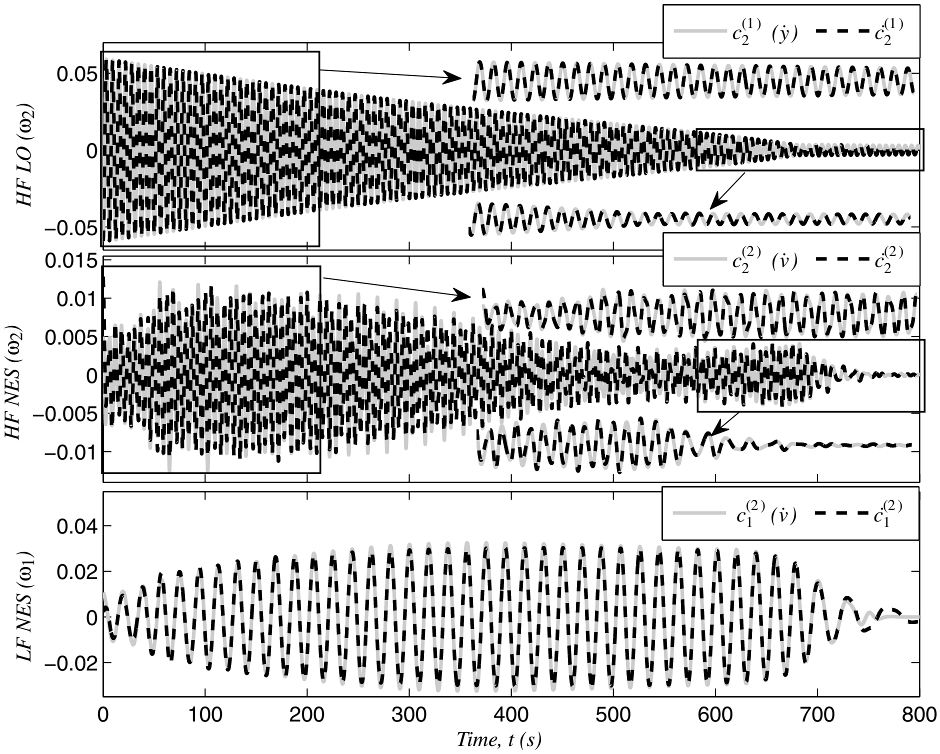

Fig. 11 Comparisons of the IMFs of the velocity time series with the derivatives of the IMFs derived from the displacement time series.

$$
\begin{aligned}
y(t) &= \frac{\psi_1^{(1)}(t) - \psi_1^{(1)*}(t)}{2j\omega_1} + \frac{\psi_1^{(2)}(t) - \psi_1^{(2)*}(t)}{2j\omega_2} \\
v(t) &= \frac{\psi_2^{(1)}(t) - \psi_2^{(1)*}(t)}{2j\omega_1} + \frac{\psi_2^{(2)}(t) - \psi_2^{(2)*}(t)}{2j\omega_2} \\
\dot{y}(t) &= \frac{\psi_1^{(1)}(t) + \psi_1^{(1)*}(t)}{2j} + \frac{\psi_1^{(2)}(t) + \psi_1^{(2)*}(t)}{2j} \\
\dot{v}(t) &= \frac{\psi_2^{(1)}(t) + \psi_2^{(1)*}(t)}{2j} + \frac{\psi_2^{(2)}(t) + \psi_2^{(2)*}(t)}{2j}
\end{aligned} \tag{43}
$$

and the accelerations can be expressed as

$$
\begin{aligned}
\ddot{y}(t) &= \dot{\psi}_1^{(1)}(t) - \frac{j\omega_1}{2}[\psi_1^{(1)}(t) + \psi_1^{(1)*}(t)] + \dot{\psi}_1^{(2)}(t) \\
&\quad - \frac{j\omega_2}{2}[\psi_1^{(2)}(t) + \psi_1^{(2)*}(t)] \\
\ddot{v}(t) &= \dot{\psi}_2^{(1)}(t) - \frac{j\omega_1}{2}[\psi_2^{(1)}(t) + \psi_2^{(1)*}(t)] + \dot{\psi}_2^{(2)}(t) \\
&\quad - \frac{j\omega_2}{2}[\psi_2^{(2)}(t) + \psi_2^{(2)*}(t)]
\end{aligned} \tag{44}
$$

Substituting into Eq. (40) and averaging out the fast terms other than $e^{j\omega_1 t}$ and $e^{j\omega_2 t}$, we obtain four complex-valued slow-flow equations in the form,

$$
\dot{\Phi}(t) = \mathbf{F}[\Phi(t)] \in \mathbb{C}^4 \tag{45}
$$

where $\Phi(t) = \{\varphi_1^{(1)}(t),\ \varphi_2^{(1)}(t),\ \varphi_1^{(2)}(t),\ \varphi_2^{(2)}(t)\}^T$ and the details of $\mathbf{F}[\Phi(t)]$ can be found in Kerschen et al. [35]. Denoted by $\tilde{y}(t)$ and $\tilde{v}(t)$, respectively, the approximate motions based on Eq. (45), in Fig. 8a we compare them to the corresponding exact responses resulting from numerical solution of Eq. (40). The approximation exhibits a reasonably good match until escape from the 1:3 transient resonance capture occurs around $t = 700$.

Now, we perform the AEMD analysis of the time series to derive the empirical slow-flow approximation by decomposing the time series into dominant components (IMFs). We express the resulting decomposition as

$$
\begin{aligned}
x_1(t) &\triangleq y(t) \approx c_1^{(1)}(t) + c_2^{(1)}(t) \\
x_2(t) &\triangleq v(t) \approx c_1^{(2)}(t) + c_2^{(2)}(t)
\end{aligned} \tag{46}
$$

where superscripts and subscripts of the IMFs indicate the DOFs and frequency components, respectively; and $0.4v_{\max}\cos\omega_0 t$ was used in performing the AEMD analysis on the NES response. Note that these notations are the opposite of those for the analytical slow-flow model (cf. Sec. IV); that is, the superscripts and subscripts imply frequency components and the DOFs in Eq. (41).

The approximate responses obtained by summing the IMFs are compared with the corresponding exact time series in Fig. 8b. As

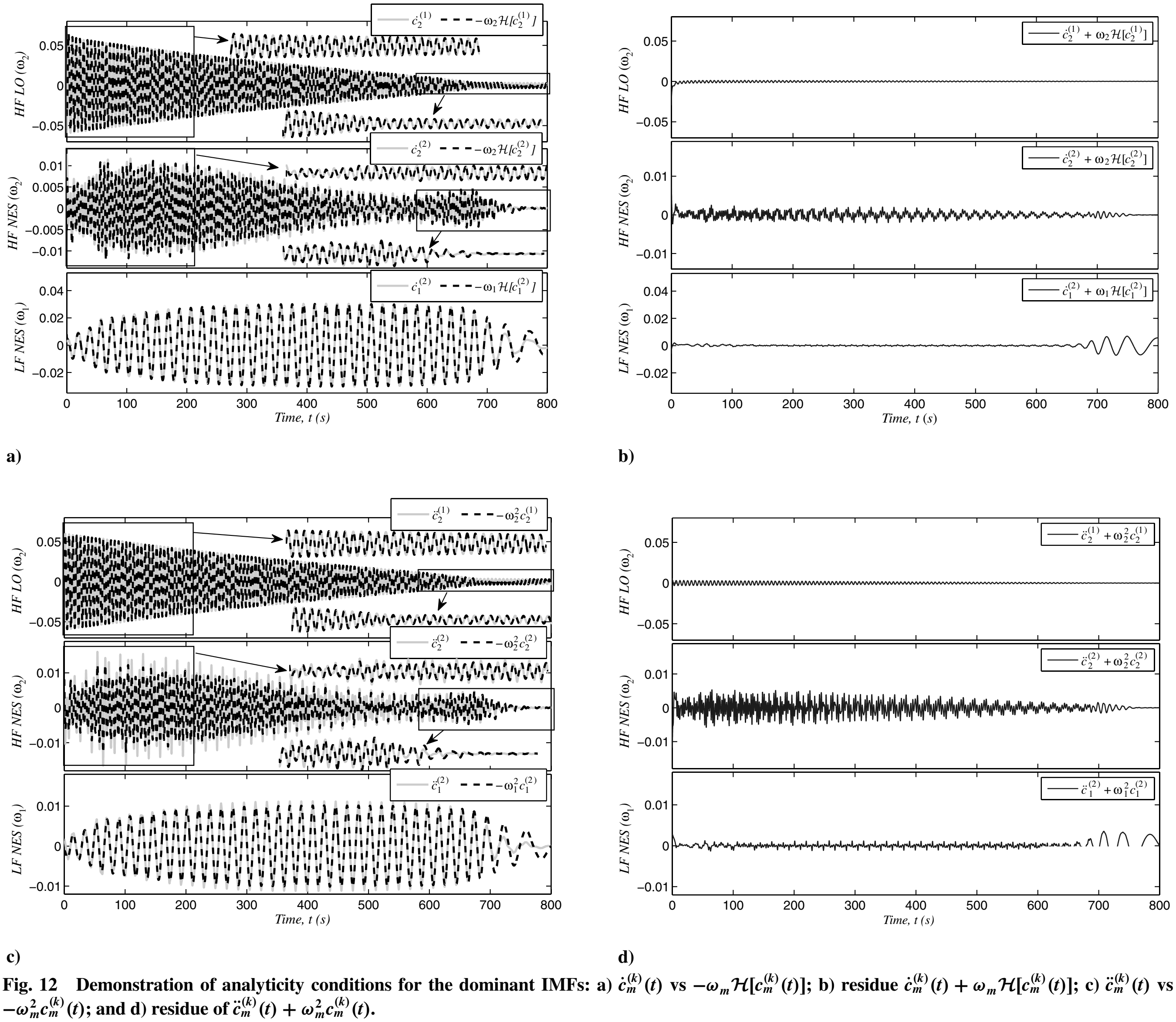

Fig. 12 **Demonstration of analyticity conditions for the dominant IMFs: a) $\dot{c}_m^{(k)}(t)$ vs $-\omega_m\mathcal{H}[c_m^{(k)}(t)]$; b) residue $\dot{c}_m^{(k)}(t) + \omega_m\mathcal{H}[c_m^{(k)}(t)]$; c) $\ddot{c}_m^{(k)}(t)$ vs $-\omega_m^2 c_m^{(k)}(t)$; and d) residue of $\ddot{c}_m^{(k)}(t) + \omega_m^2 c_m^{(k)}(t)$.**

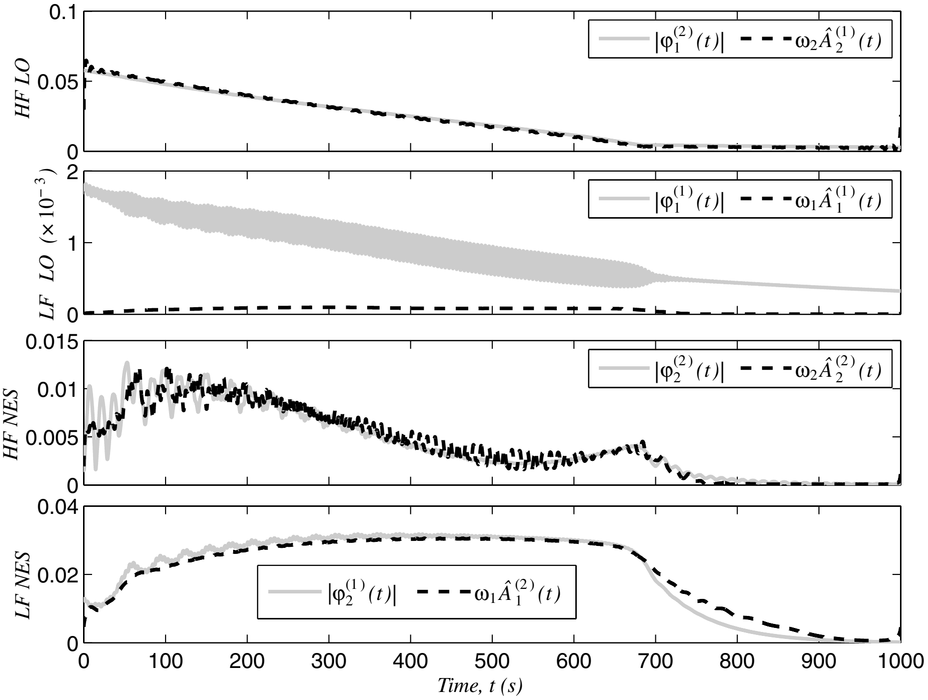

Fig. 13 Comparison of the envelopes of the analytical and empirical slow-flow models.

addressed in Sec. III, the IMF-based approximations exhibit a better match with the original dynamics by virtue of the ad hoc decomposition method. The analytical slow flow deviates from the original time series as soon as the dynamics exhibits escape from resonance (i.e., the analytical slow-flow model derived from averaging loses its validity when escape from resonance occurs). On the other hand, the EMD method tends to separate frequency components between the individual IMFs as long as the corresponding frequency ratios satisfy the narrowband conditions.

Figure 9 compares the components of the analytical and empirical decompositions. Except for the LF component of the LO, the analytical slow-flow model matches well with the IMFs. The deviations in the LF LO components indicate that this component does not make a significant contribution to the nonlinear modal interactions due to 1:3 transient resonance capture; and also that either the analytical or the empirical decomposition is spurious. While the IMF (although of small amplitude) possesses frequency content near $\omega_1 = \omega_0/3$ (cf. the bottom wavelet transform spectrum plot in Fig. 9b), the analytical slow flow contains high-frequency terms. We conjecture that this happens because we employed optimal but nonunique initial conditions to solve the slow-flow model (45) according to the formulation developed in Kerschen et al. [35].

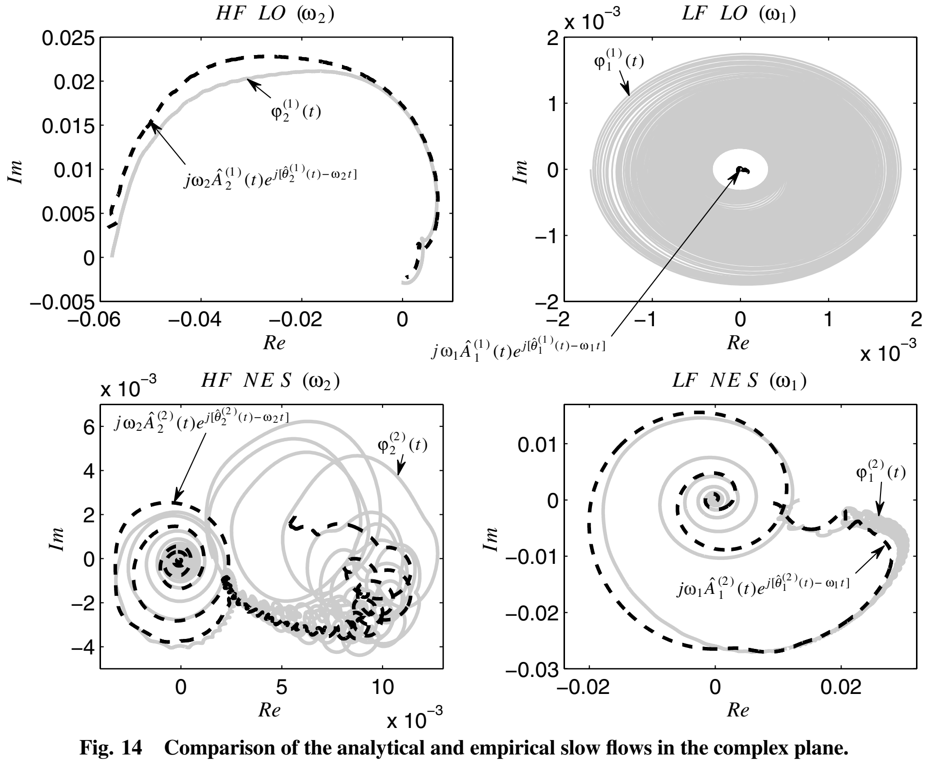

Fig. 14 Comparison of the analytical and empirical slow flows in the complex plane.

Therefore, this analytical LF LO component can be regarded as being spurious and nonphysical.

In Fig. 10a we compare the exact velocity time series, $\dot{y}(t)$ and $\dot{v}(t)$ from Eq. (40), with their approximate solutions given by Eq. (43), which demonstrates again the validity of the analytical slow-flow model. We note that the HF component (i.e., at $\omega_2 = \omega_0$) of the NES becomes amplified, appearing prominent during the initial transients, in particular. In addition, the AEMD was applied directly to the velocity time series and the resulting IMFs are compared with the components derived from the CX-A technique (Fig. 10b). Similar to the case of the displacements, all velocity components of the analytical and empirical slow flows show compatibility except for the LF LO components.

Based on the previous results, from here on we consider the HF LO and the HF and LF NES components as the dominant slow flows that govern 1:3 transient resonance capture in the coupled oscillator (40). Before we further examine the equivalence between the analytical and empirical slow flows, we examine the analyticity condition by the dominant IMFs. To check the relation (30) that results from the analyticity condition (29), the IMFs for the displacements (that is, $c_2^{(1)}(t)$ and $c_{1,2}^{(2)}(t)$) are numerically differentiated, and the resulting high-frequency noise is eliminated by applying a low-pass filter with a cutoff frequency of $0.7\omega_2$. Such noisy signals are produced by numerical differentiation and depend on the step size of the time series. When compared with the IMFs obtained directly from the velocities (cf. Fig. 11), the numerically differentiated IMFs from the displacement data exhibit a reasonably good match. This investigation demonstrates one of the analytic properties for well-decomposed IMFs, implying that the measurement of displacements in the time domain can be used for establishing a slow-flow model in terms of both displacement and velocity decompositions.

Other properties of analyticity of the IMFs are examined in Fig. 12, checking the analyticity conditions (29) and (38). Comparisons of the quantities $\dot{c}_m^{(k)}(t)$ and $-\omega_m \mathcal{H}[c_m^{(k)}(t)]$, and of $\ddot{c}_m^{(k)}(t)$ and $-\omega_m^2 c_m^{(k)}(t)$, show reasonable compatibility. Here, direct differentiation of the dominant IMFs from the displacement data was used, although the IMFs from the velocities and accelerations could be used as well. Some nonnegligible residues are observed for the HF NES component; however, it is suspected that they appear due to errors introduced by the numerical differentiations that survive even after application of low-pass filtering (cf. the noisy content in the residues). These residues can be neglected, because such discrepancies may exist even if two time series possess slight phase differences between them or if they are not pointwise coincident.

Another interesting observation from the residues of the HF LO and LF NES components is that the dynamics of 1:3 transient resonance capture behaves as if the two oscillators (the LO and NES) are uncoupled (an observation also made in Kerschen et al. [35]). The first and third plots in Fig. 12d demonstrate that this uncoupling approximately holds because $\ddot{c}_2^{(1)}(t) + \omega_2^2 c_2^{(1)}(t) \approx 0$ and $\ddot{c}_1^{(2)}(t) + \omega_1^2 c_1^{(2)}(t) \approx 0$, respectively. Noting that $c_2^{(1)}(t)$ and $c_1^{(2)}(t)$ are the dominant IMFs for the nonlinear modal interactions through 1:3 transient resonance capture, we deduce in turn that $\ddot{y}(t) + \omega_0^2 y(t) \approx 0$ and $\ddot{v}(t) + (\omega_0/3)^2 v(t) \approx 0$, a result that fully confirms the findings in Kerschen et al. [35].

Now we examine the equivalence between the analytical slow-flow model and the dominant IMFs. Recalling Eq. (34), we note that, by virtue of the analyticity of proper IMFs, the slow flow can be expressed approximately as

$$\varphi_k^{(m)}(t) \approx j\omega_m \hat{A}_m^{(k)}(t) e^{j\theta_m^{(k)}(t)} \tag{47}$$

where $\varphi_k^{(m)}(t)$ can be obtained from the analytical slow-flow model, and $\hat{A}_m^{(k)}(t)$ and $\theta_m^{(k)}(t) = \hat{\theta}_m^{(k)}(t) - \omega_m t$ are computed by extracting the slow components of the dominant IMFs; the indices m and k denote the frequency component and of the DOF, respectively.

Figure 13 compares the slowly varying envelopes derived from the analytical slow flow and the slow components of dominant IMFs; that is, we compare the amplitudes $|\varphi_k^{(m)}(t)|$ and $\omega_m \hat{A}_m^{(k)}(t)$, where $\hat{A}_m^{(k)}(t)$ is evaluated from Eq. (25). Again, except for the LF LO component, the slow envelopes of the analytical slow flow and the dominant IMFs agree well. Moreover, the analytical and empirical slow flows (that is, $\varphi_k^{(m)}(t)$ and $j\omega_m \hat{A}_m^{(k)}(t) e^{j\theta_m^{(k)}(t)}$) are compared directly in the complex plane to check as well the validity of the slow phases of corresponding components of the IMFs (Fig. 14). To perform this comparison, we compute the phases $\hat{\theta}_m^{(k)}(t)$ of the dominant IMFs by Eq. (25) and then subtract from them the respective fast phases $\omega_m t$ to derive the slowly varying phases $\theta_m^{(k)}(t)$; in addition, low-pass filters with cutoff frequencies equal to $0.7\omega_m$ were applied to the results. The comparison in the complex plane clearly demonstrates the close correspondence between the analytical slow

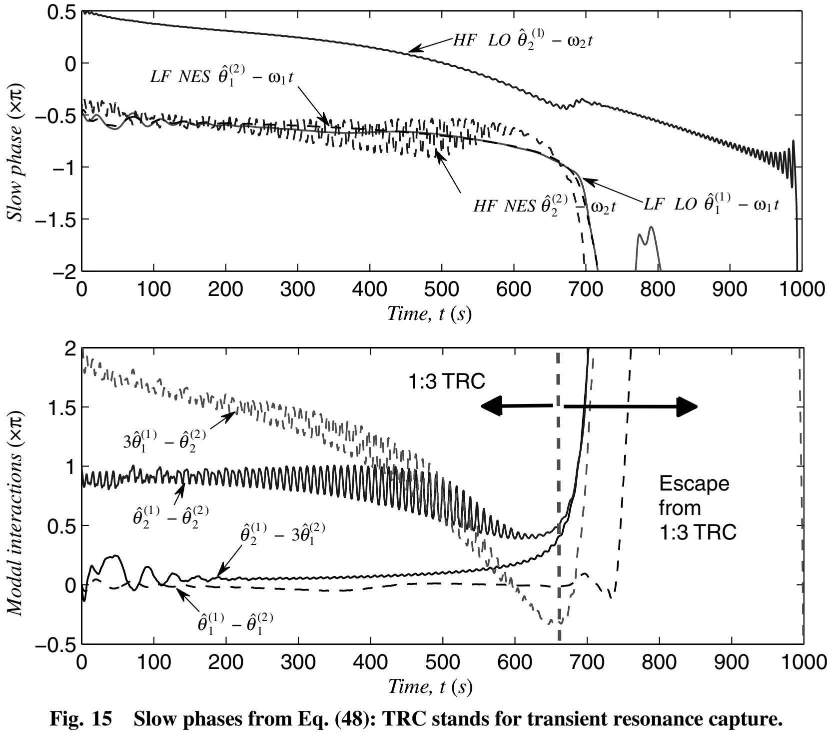

Fig. 15 Slow phases from Eq. (48): TRC stands for transient resonance capture.

flow and the slow components of the dominant IMFs, thus validating the previous theoretical formulation and providing a physical interpretation of the EMD results.

Finally, we explore the equivalence between the analytical and empirical slow-flow models by studying in more detail the 1:3 transient resonance capture in the transient dynamics in the system of coupled oscillators (40). Considering first the analytical slow flow derived by the CX-A method by expressing Eq. (45) in polar form, we can obtain a set of real-valued modulation equations in terms of slow amplitudes and slow phase differences (see Kerschen et al. [35] for details). Similarly, one can consider an analogous expression for the slow flow derived from the dominant IMFs, which can be mathematically written in the form

$$\dot{\mathbf{a}} = \mathbf{f}(\mathbf{a}, \phi), \qquad \dot{\phi} = \mathbf{g}(\mathbf{a}, \phi) \tag{48}$$

where $\mathbf{a} = \{\hat{A}_2^{(1)}(t), \hat{A}_1^{(2)}(t), \hat{A}_2^{(2)}(t)\}^T$ and $\phi = \{\phi_{11}, \phi_{22}, \phi_{21}\}^T$. Here, the phase difference ϕ_{ij} is defined only for the nontimelike (i.e.,

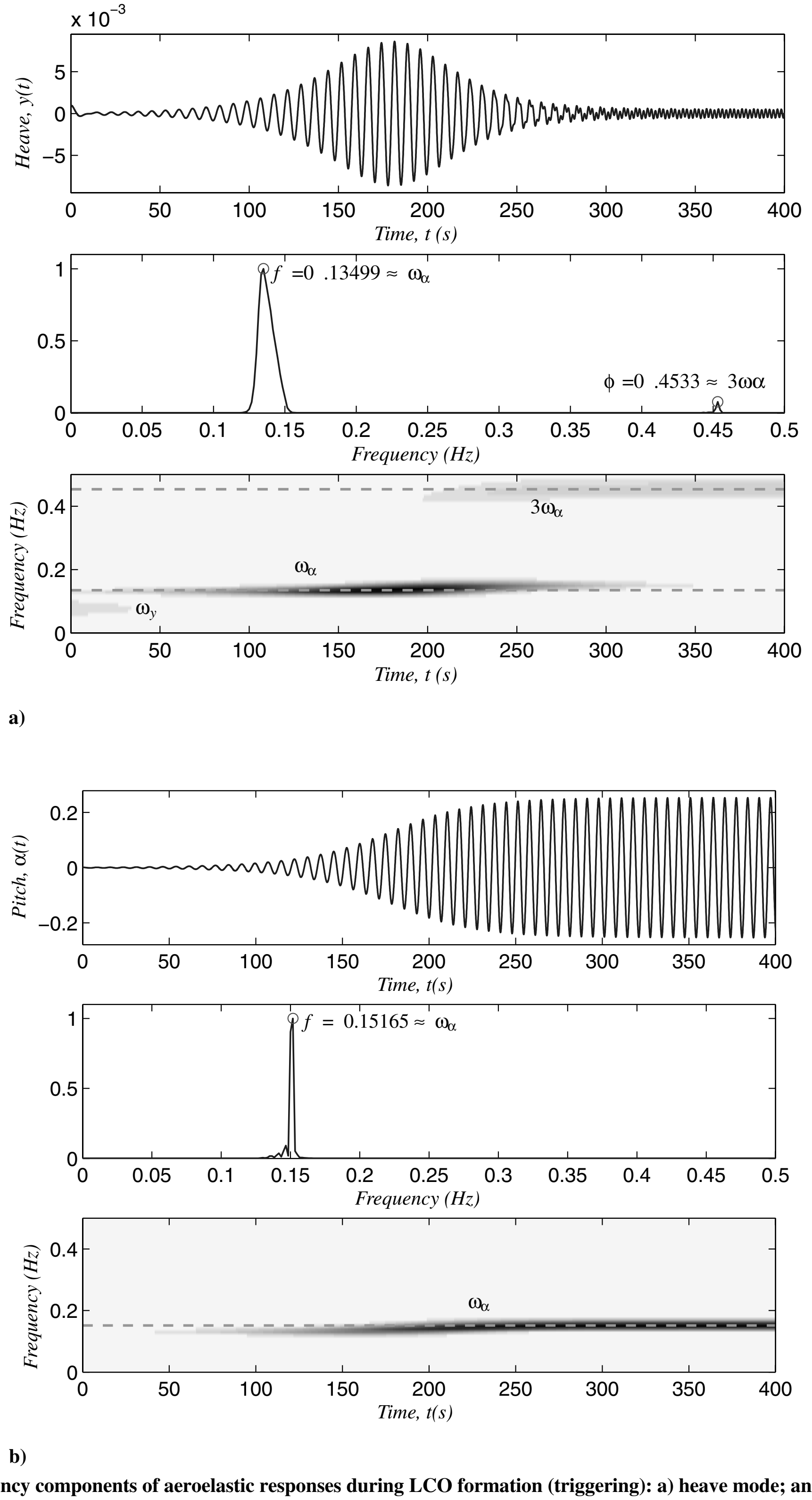

Fig. 16 Frequency components of aeroelastic responses during LCO formation (triggering): a) heave mode; and b) pitch mode.

nearly constant with respect to fast time scale in average) phase variables, because timelike (i.e., monotonic dependence on time on average) phases can always be averaged out of the dynamics. Hence, we define the IMF-based slow phase differences as $\phi_{11} \triangleq \theta_1^{(1)} - \theta_1^{(2)}$, $\phi_{22} \triangleq \theta_2^{(1)} - \theta_2^{(2)}$, and $\phi_{21} \triangleq \theta_2^{(1)} - 3\theta_1^{(2)}$.

The plots of the slow amplitudes $\dot{\mathbf{a}}$ were already presented in Fig. 13, and the IMF-based slow phases $\theta_m^{(k)}(t) = \hat{\theta}_m^{(k)}(t) - \omega_m t$ are depicted in Fig. 15. We note that the slopes for the slow phases appear almost constant on average (i.e., $\dot{\theta}_m^{(k)}(t) \approx -\omega_m$) with respect to time while the two oscillators are engaged in 1:3 transient resonance capture (i.e., until $t \approx 650$). Recall from Sec. IV that the computation of the instantaneous frequencies yields the dominant frequency values ω_m for proper IMFs, which implies that the slow phases are constant on average with respect to the fast time scale. We proved that

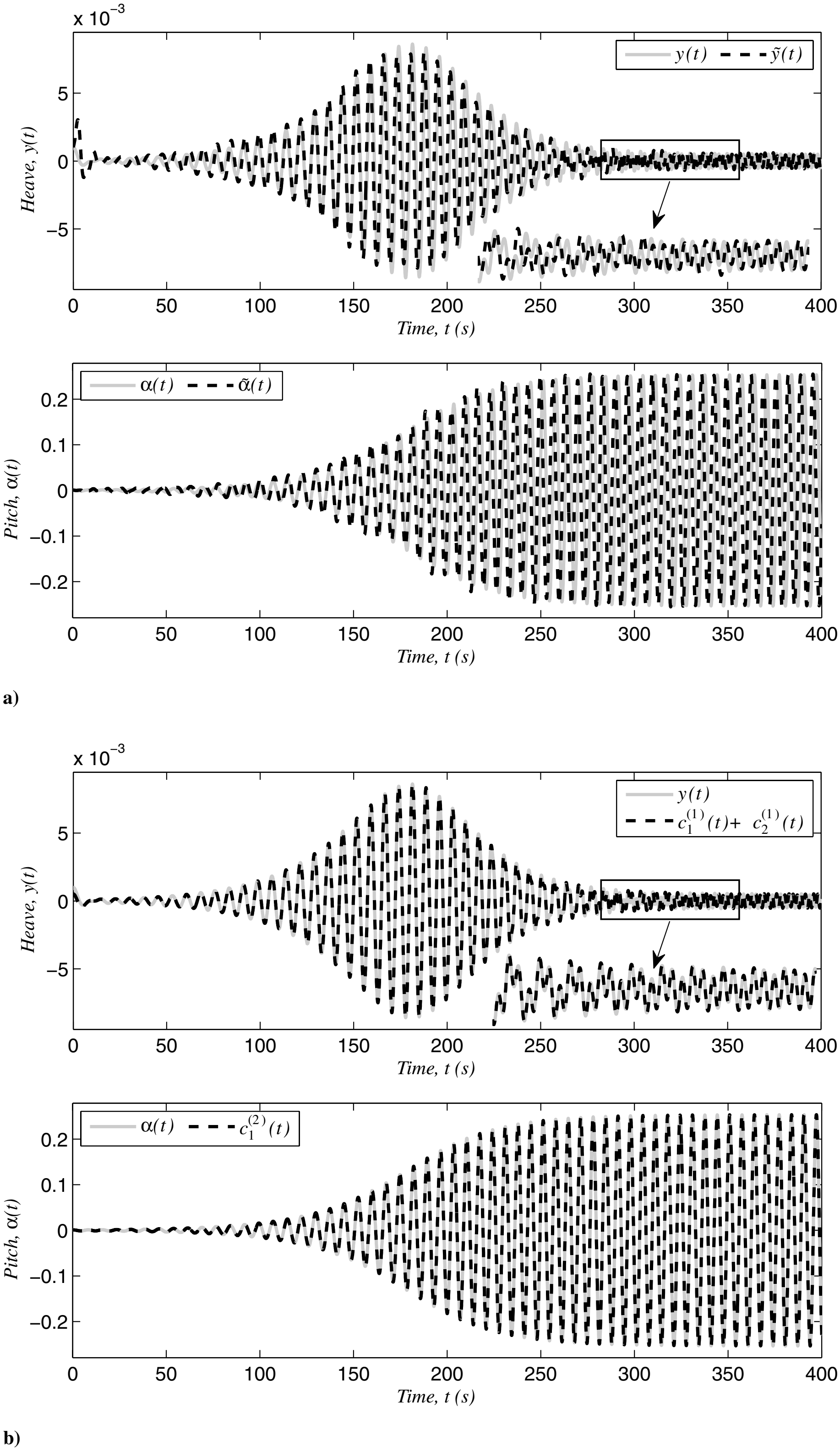

Fig. 17 Comparison of the exact numerical responses with corresponding approximate responses derived from a) analytical; and b) empirical slow flows.

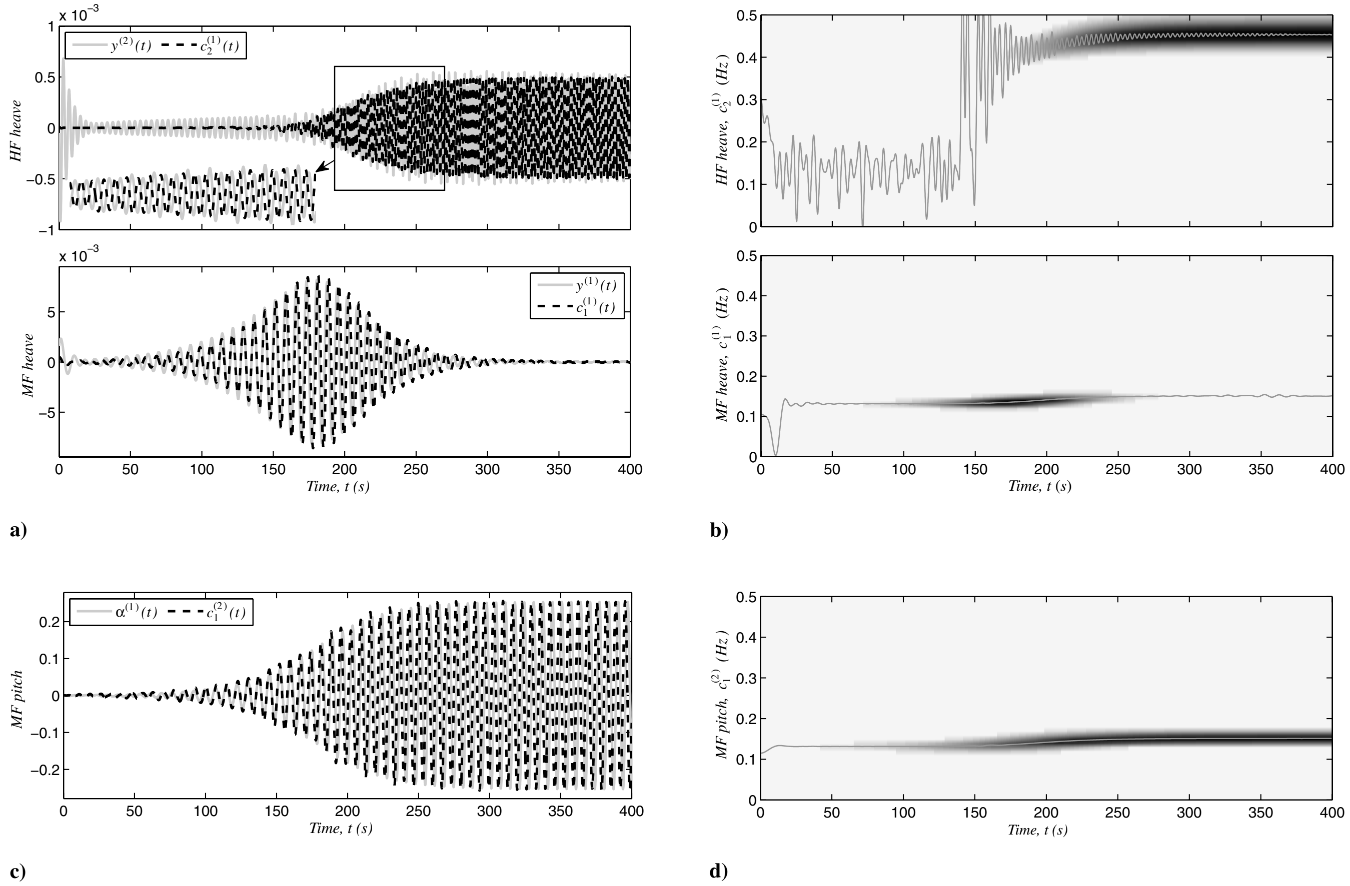

a) **b)** **c)** **d)**

Fig. 18 Comparison of respective frequency components of responses derived from the analytical slow flow and AEMD (parts a and c); and corresponding wavelet spectra of exact responses superimposed on the instantaneous frequencies of the IMFs (parts b and d).

this relation does not hold if the slow amplitudes are no longer slow with respect to the time scales of the respective dominant (fast) frequencies of the responses; that is, when the slow amplitude variables exhibit timelike behavior.

The phase differences ϕ_{ij}, $i, j = 1, 2$ are depicted also in Fig. 15, from which we note that $\phi_{12} \triangleq 3\theta_1^{(1)} - \theta_2^{(2)}$ is a timelike variable, which explains why it should not be included in (48) (because it can be averaged out of the dynamics and does not contribute in the 1:3

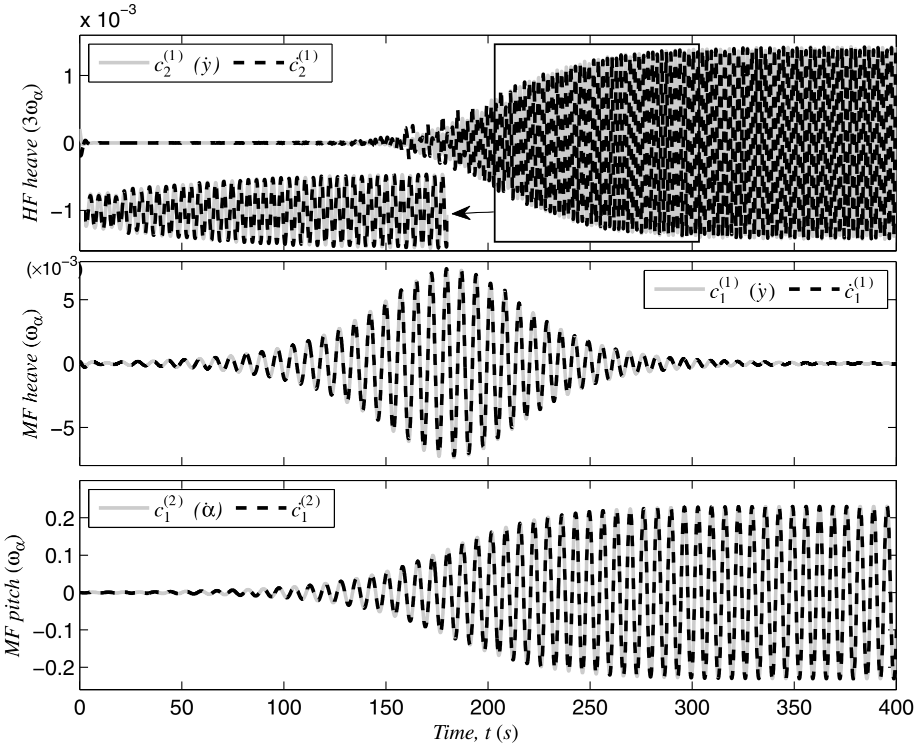

Fig. 19 Comparison between the IMFs derived from velocity time series and the derivatives of the IMFs derived from displacement time series.

transient resonance capture). On the other hand, the other phase differences exhibit nontimelike behaviors until $t \approx 650$, evidence of the engagement of the corresponding modes in 1:3 transient resonance capture. Finally, the timelike behaviors of the slow phase differences after $t \approx 650$ indicate escape from resonance capture. All these EMD-based observations were theoretically investigated in Kerschen et al. [35], and so these results provide direct numerical confirmation of the analytical results reported in that work.

B. Triggering Mechanism of Aeroelastic Instability

As a second application, we demonstrate the equivalence of the analytical slow flow and EMD for the triggering mechanism of limit cycle oscillations (LCOs) of a rigid wing in flow studied in Lee et al. [36]. The nondimensionalized aeroelastic equations of motion of this system are written as,

$$\ddot{y} + x_\alpha\ddot{\alpha} + \mu C_{L,\alpha}\Theta\dot{y} + \Omega^2 y + \xi_y y^3 + \mu C_{L,\alpha}\Theta^2\alpha = 0$$
$$r_\alpha^2\ddot{\alpha} + x_\alpha\ddot{y} - \mu\gamma C_{L,\alpha}\Theta\dot{y} + (r_\alpha^2 - \mu\gamma C_{L,\alpha}\Theta^2)\alpha + \xi_\alpha\alpha^3 = 0 \quad (49)$$

where y and α are heave and pitch responses of the wing, respectively; dots denote differentiation with respect to nondimensional time; and all the other system parameters are as given in Lee et al. [36]. Note that, although all quantities in the this aeroelastic model are nondimensional, the units for time and frequency will be assigned as s and Hz (or rad/s), respectively, for the purpose of easy interpretation.

Typical LCO formation for this system is depicted in Fig. 16, for zero initial conditions except the heave displacement $y(0) = 0.001$, at reduced velocity $\Theta = 0.95 > \Theta_{\text{Flutter}} = 0.87$. Fourier analysis shows that the heave mode contains two dominant frequencies at $\omega_\alpha = 1$ and $3\omega_\alpha$ (rad/s), and that the pitch mode possesses a single dominant frequency at ω_α. Referring to Fig. 16, we note that the wavelet analysis provides the temporal evolutions of these dominant harmonics. The heave mode, initially excited at its uncoupled linear natural frequency $\omega_y = \Omega = 0.5$, exhibits transitions to ω_α and then to $3\omega_\alpha$, and the pitch mode remains near its uncoupled linearized natural frequency ω_α throughout the formation of the LCO.

The triggering mechanism for this type of aeroelastic instability consists of three stages [36]: initial excitation by the flow of the heave mode through which 1:1 transient resonance capture triggers the pitch mode; escape from the 1:1 transient resonance capture; and final transition to 3:1 permanent resonance capture, at which point the LCO is fully developed. Numerical and analytical investigations of LCO triggering and formation have been carried out in Lee et al. [36], and here we focus on the equivalence of the analytical slow flow to the dominant IMFs obtained from empirical decomposition.

First, we review the derivation of the analytical slow flow performed in Lee et al. [36]. From the time-frequency analysis in Fig. 16,

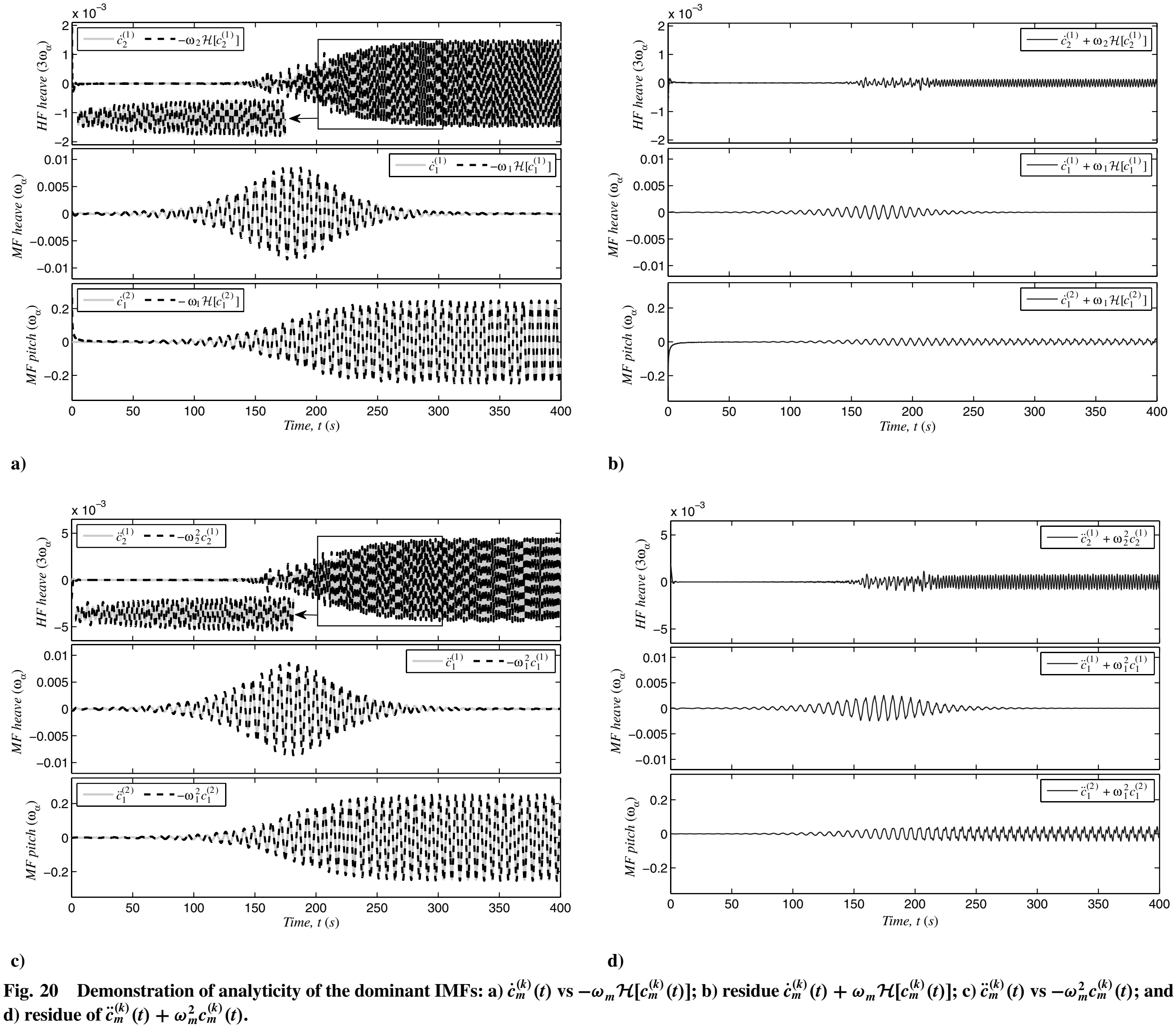

a)

b)

c)

d)

Fig. 20 Demonstration of analyticity of the dominant IMFs: a) $\dot{c}_m^{(k)}(t)$ vs $-\omega_m\mathcal{H}[c_m^{(k)}(t)]$; b) residue $\dot{c}_m^{(k)}(t) + \omega_m\mathcal{H}[c_m^{(k)}(t)]$; c) $\ddot{c}_m^{(k)}(t)$ vs $-\omega_m^2 c_m^{(k)}(t)$; and d) residue of $\ddot{c}_m^{(k)}(t) + \omega_m^2 c_m^{(k)}(t)$.

we expect that at least three fast frequencies (ω_y, ω_α, $3\omega_\alpha$) are required for an accurate slow-flow model. Using the notations introduced in Sec. II, we assume that the heave and pitch modes can be decomposed as

$$\begin{aligned} x_1(t) &\triangleq y(t) = y^{(0)}(t) + y^{(1)}(t) + y^{(2)}(t), \\ x_2(t) &\triangleq \alpha(t) = \alpha^{(0)}(t) + \alpha^{(1)}(t) + \alpha^{(2)}(t) \end{aligned} \tag{50}$$

where superscript and subscript conventions were defined in the previous sections. The superscripts for the decomposition indicate the components associated with ω_0, ω_1, and ω_2, respectively, where $\omega_0 = \omega_y = \Omega = 0.5$, $\omega_1 = \omega_\alpha = 1$, and $\omega_2 = 3\omega_\alpha$ (rad/s). The aforementioned three frequency components are referred to as low-frequency (LF, ω_0), middle-frequency (MF, ω_1), and high-frequency (HF, ω_2) components, respectively [36].

Introducing the six complex variables,

$$\begin{aligned} \psi_1^{(0)}(t) &= \dot{y}^{(0)}(t) + j\omega_0 y^{(0)}(t) \equiv \varphi_1^{(0)}(t)e^{j\omega_0 t} \\ \psi_2^{(0)}(t) &= \dot{\alpha}^{(0)}(t) + j\omega_0 \alpha^{(0)}(t) \equiv \varphi_2^{(0)}(t)e^{j\omega_0 t} \\ \psi_1^{(1)}(t) &= \dot{y}^{(1)}(t) + j\omega_1 y^{(1)}(t) \equiv \varphi_1^{(1)}(t)e^{j\omega_1 t} \\ \psi_2^{(1)}(t) &= \dot{\alpha}^{(1)}(t) + j\omega_1 \alpha^{(1)}(t) \equiv \varphi_2^{(1)}(t)e^{j\omega_1 t} \\ \psi_1^{(2)}(t) &= \dot{y}^{(2)}(t) + j\omega_2 y^{(2)}(t) \equiv \varphi_1^{(2)}(t)e^{j\omega_2 t} \\ \psi_2^{(2)}(t) &= \dot{\alpha}^{(2)}(t) + j\omega_2 \alpha^{(2)}(t) \equiv \varphi_2^{(2)}(t)e^{j\omega_2 t} \end{aligned} \tag{51}$$

the original variables can be expressed in terms of them. Substituting into Eq. (49) and averaging out fast terms other than those corresponding to the three fast oscillations, $e^{j\omega_0 t}$, $e^{j\omega_1 t}$, and $e^{j\omega_2 t}$, we finally obtain a set of six slow-flow equations, which constitute the slow flows describing aeroelastic instability triggering and formation in this system.

$$\dot{\Phi}(t) = \mathbf{F}(\Phi(t)) \in \mathbb{C}^6 \tag{52}$$

where $\Phi(t) = \{\varphi_1^{(0)}(t),\ \varphi_2^{(0)}(t),\ \varphi_1^{(1)}(t),\ \varphi_2^{(1)}(t),\ \varphi_1^{(2)}(t),\ \varphi_2^{(2)}(t)\}^T$ is the vector of complex amplitudes, and the details of the complex-valued function $\mathbf{F}(\Phi(t))$ can be found in Lee et al. [36].

Using optimal initial conditions in the sense discussed in Vakakis et al. [32] for the modulation Eqs. (52), the approximate solutions $\tilde{y}(t)$ and $\tilde{\alpha}$ are compared with the original time series $y(t)$ and $\alpha(t)$, in Fig. 17a. We note that except for the initial transients the solutions for the analytical slow-flow model approximate well the exact numerical solutions.

Performing AEMD analysis with $0.2y_{\max}\cos 3\omega_\alpha t$ as a masking signal only to the heave mode response, we obtain two dominant IMFs (for the MF and HF components) for the heave mode, and a single IMF (for the MF component) for the pitch mode. Express the resulting empirical decomposition as

$$x_1(t) \triangleq y(t) \approx c_1^{(1)}(t) + c_2^{(1)}(t), \qquad x_2(t) \triangleq \alpha(t) \approx c_1^{(2)}(t) \tag{53}$$

where $c_0^{(1)}(t)$ (the LF heave), $c_0^{(2)}(t)$ and $c_2^{(2)}(t)$ (the LF and HF pitch) are omitted in Eq. (53) as spurious. This result is consistent with the Fourier and wavelet transform results depicted in Fig. 16. These empirical decompositions are compared with the original time series in Fig. 17b, and are found to approximate the original time series better than the analytical slow-flow model. Note that in this case both the analytical and empirical slow-flow models are valid over the entire time span, whereas the analytical slow flow in Sec. V.A was valid only until escape from 1:3 transient resonance capture occurred.

The dominant IMFs for the aeroelastic modes are compared with the corresponding analytical approximations in Fig. 18. In general, the slow components of the dominant IMFs are reasonably compatible with the results of the analytical slow flow, except for some discrepancies in the initial stage of the responses. We note that the dominant IMFs carry more accurate and physically meaningful information by virtue of their numerical construction, compared with the analytical slow-flow results that were derived under certain assumptions, the most important of which were the slow–fast partition of the dynamics and the composition of the dynamics by distinct harmonic components. As noted in Lee et al. [36], one of the reasons the discrepancies between the EMD and analytical slow flow occur is that the slow-flow model (52) possesses higher dimensionality than the original dynamical system (in fact, the dimensionality of the slow-flow model is dictated by the number of dominant harmonics in the transient dynamics). As a result, the initial conditions for (52) were obtained as solutions of an optimization problem [32] and are not unique. Also, we remark that the comparisons in Figs. 17 and 18 suggest the possibility of deriving an

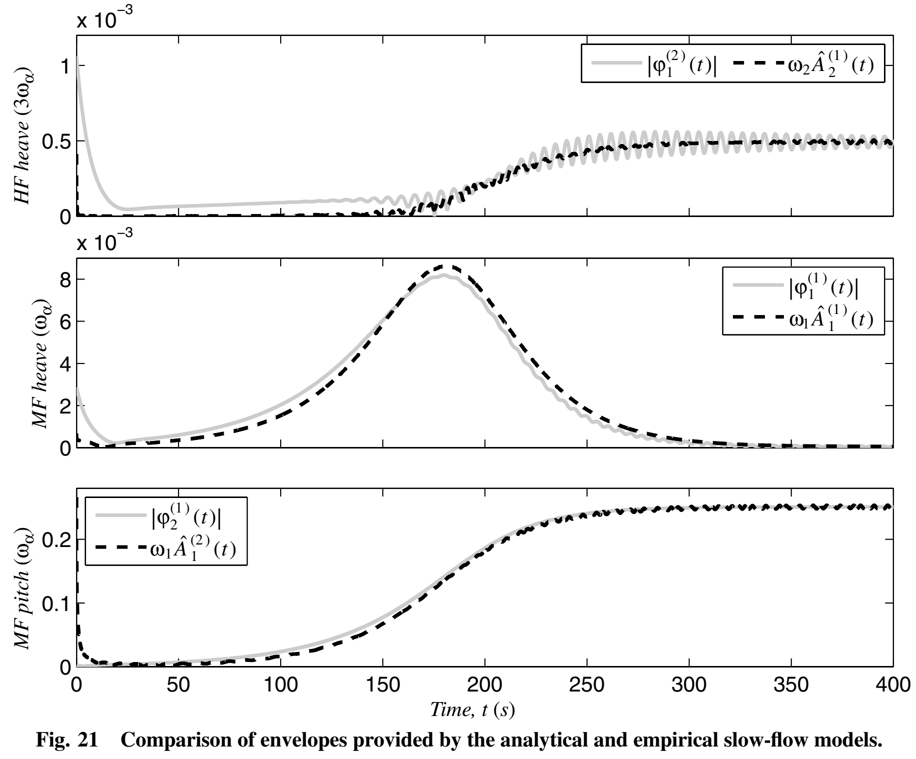

Fig. 21 Comparison of envelopes provided by the analytical and empirical slow-flow models.

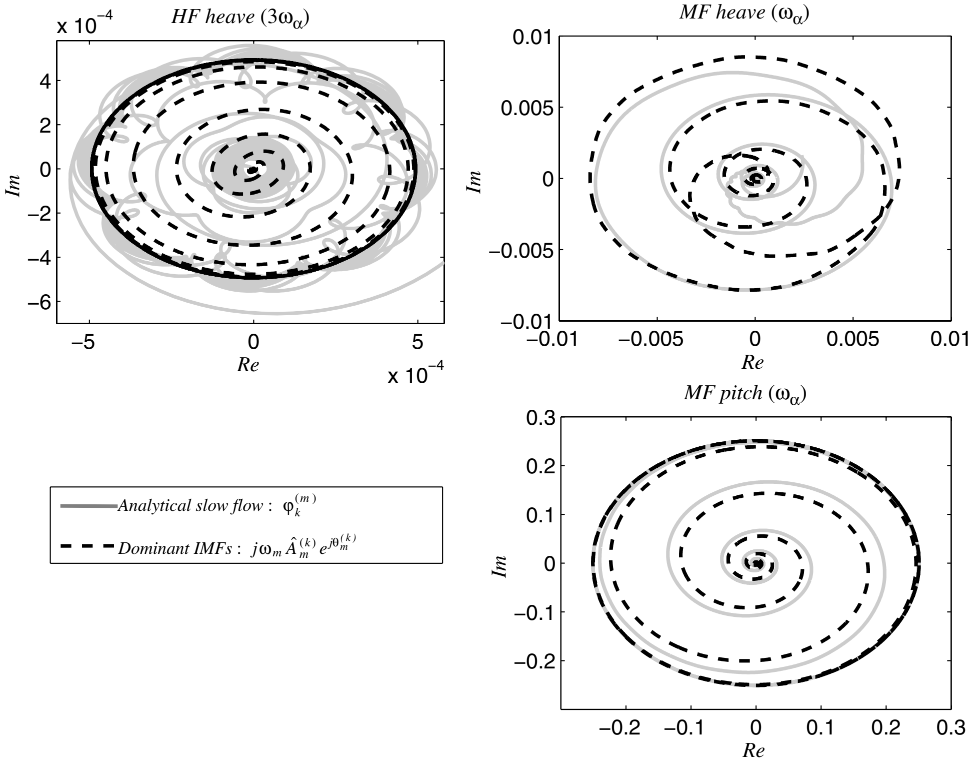

Fig. 22 Comparison of analytical and empirical slow flows in the complex plane.

analytical slow-flow model with the two dominant frequencies of the MF and HF components (i.e., a two-frequency averaged system), but this will not be further discussed in this paper.

In Fig. 19 the IMFs for the displacements are numerically differentiated and compared with those directly obtained from velocity time series, which demonstrates the analytic equivalence (30) between the analytical slow flow and the slow components of the dominant IMFs. There exist, however, discrepancies in the HF heave component around $t \in [150, 200]$, where the escape from 1:1 transient resonance capture and transition to 3:1 permanent resonance capture occurs.

Additional analytic properties of the IMFs are examined in Fig. 20 based on the analyticity relations (29) and (38). From these results we note that the residues in $\dot{c}_m^{(k)} + \omega_m \mathcal{H}[c_m^{(k)}]$ and $\ddot{c}_m^{(k)} + \omega_m^2 c_m^{(k)}$ appear rather significant in this comparison. These residues can still be neglected (i.e., the assumption of fast harmonic dynamics in Eq. (38) is still valid), because in this case they are due to differences in the frequencies used for the slow-flow model; that is, whereas the frequencies for the MF and HF components in the analytical slow-flow model were $\omega_1 = 1$ and $\omega_2 = 3$ (rad/s), the dominant frequencies in Fig. 16 are $0.1350 \times 2\pi = 0.848$ and $0.4533 \times 2\pi = 2.848$ (rad/s) for the heave mode, and $0.1516 \times 2\pi = 0.953$ (rad/s) for the pitch mode. These differences can be further amplified during differentiation.

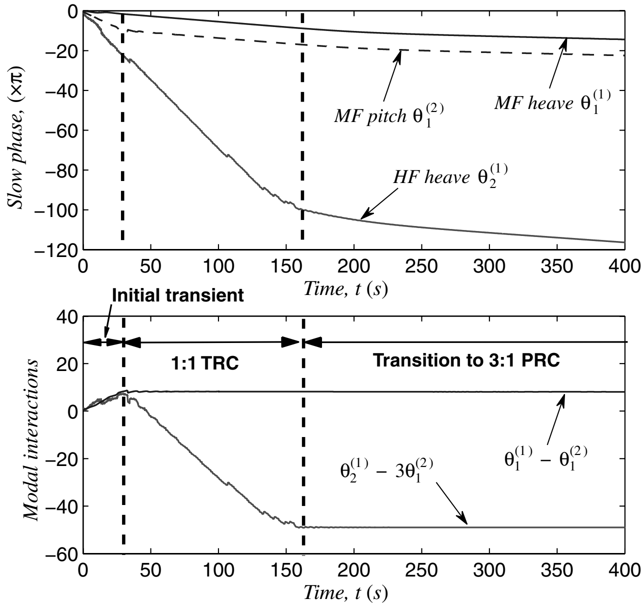

Fig. 23 Slow phases and phase differences indicating the occurrence of nonlinear modal interactions; PRC stands for permanent resonance captures.

Now we examine the equivalence between the (analytical) slow-flow model and the slow components of the dominant IMFs; that is, we wish to test the equivalence between the analytical slow-flow and the numerical AEMD results. This is determined by the relation $\varphi_k^{(m)}(t) \approx j\omega_m \hat{A}_m^{(k)}(t) e^{j\theta_m^{(k)}(t)}$ in Eq. (47), where $\varphi_k^{(m)}(t)$ is obtained from the analytical slow-flow model, and the slowly varying amplitude and phase, $\hat{A}_m^{(k)}(t)$ and $\theta_m^{(k)}(t)$, are computed directly from the dominant IMFs. Figures 21 and 22 compare the slowly varying envelopes $|\varphi_k^{(m)}(t)|$ and $\omega_m \hat{A}_m^{(k)}(t)$, and the respective slow flows in the complex plane. We verify that, except for a slight phase deviation, the analytical slow flow correlates closely with the dominant IMFs (i.e., the empirical slow flow).

Finally, the slow phases $\theta_m^{(k)}(t)$ derived from the IMFs are presented in the upper plot of Fig. 23. Unlike the two-DOF system of coupled oscillators considered in Sec. V.A, the slopes of all the slow-phase variables exhibit clear linearity. The differences between the slow phases exhibit nontimelike behaviors in the regimes of nonlinear modal interactions that are due to 1:1 transient resonance capture (i.e., the phase difference $\theta_1^{(1)} - \theta_1^{(2)}$) or to 3:1 permanent resonance capture (i.e., the phase difference $\theta_2^{(1)} - 3\theta_1^{(2)}$) as depicted in the lower plot of Fig. 23. Moreover, these observations are consistent with the analytical findings reported in Lee et al. [36].

VI. Conclusions

We have provided a physics-based interpretation of proper IMFs derived by EMD in terms of slow flows governing the dynamics of oscillatory time series. By proper IMFs we mean those IMFs that satisfy certain narrowband restrictions and near-analyticity conditions. To study the derivation of proper IMFs, we proposed an enhancement of the EMD procedure through the use of masking signals, leading to an advanced EMD (AEMD) procedure. Key to our discussion of equivalence between slow-flow dynamics and IMFs was a discussion of the issue of analyticity of the derived IMFs, which implies equivalence of the EMD decomposition and a similar decomposition derived by the analytical CX-A method. Decomposition of an IMF in terms of slow and fast components and harmonic dependence with respect to the fast time scale implies analyticity of that IMF. As shown in the examples considered in this work, in practical applications such analyticity conditions are only approximately satisfied. Nevertheless, the outlined formulations provide a theoretical framework for EMD, which previously was considered to be entirely ad hoc, lacking any theoretical basis. Indeed, as shown in this work, proper IMFs can be interpreted as being the responses of the slow-flow dynamics of an oscillatory process. This paves the way for employing EMD as the basis for the development of a nonlinear, nonparametric system identification and reduced-order modeling technique that will 1) be based on direct analysis of measured time series data, 2) be capable of analyzing the strongly nonlinear, complex dynamics of multicomponent systems, and 3) hold promise to be as utilitarian as the well-established experimental modal analysis is for linear systems. As such, the proposed methodology will be applicable to a broad class of time-variant or time-invariant, linear or nonlinear, and smooth or nonsmooth dynamical systems. The development of this method is the focus of another paper [30].

Appendix: Open Issues: Limitations of the Empirical Mode Decomposition Method

As has been addressed by many researchers [10,21–25], the most serious limitation of the EMD method is the difficulty separating the components that contain closely spaced modes. To demonstrate this, we regenerate some plots in Deering and Kaiser [27].

The standard EMD is applied to a signal $x(t) = A_1 \sin(2\pi f_1 t) + A_2 \sin(2\pi f_2 t)$, where $A_1 = A_2 = 1$, $f_1 = 1$ Hz, and f_2 varies from 0.1 to 3 Hz. Nominally, the resulting IMFs should be $c_1(t) = A_1 \sin(2\pi f_1 t)$ $(c_1(t) = A_2 \sin(2\pi f_2 t))$ and $c_2(t) = A_2 \sin(2\pi f_2 t)$ $(c_2(t) = A_1 \sin(2\pi f_1 t))$ when $f_1 < f_2$ $(f_1 > f_2)$. The computations in Deering and Kaiser [27] used the central difference scheme for the approximation to the time derivatives. The first two dominant frequency components are extracted by means of the standard EMD, followed by the computation of the instantaneous frequencies, $\hat{f}_1$ and $\hat{f}_2$, and the (mean) amplitudes, $\hat{A}_1$ and $\hat{A}_2$, with maximum and minimum variations at a time instant away from the end-effect zones.

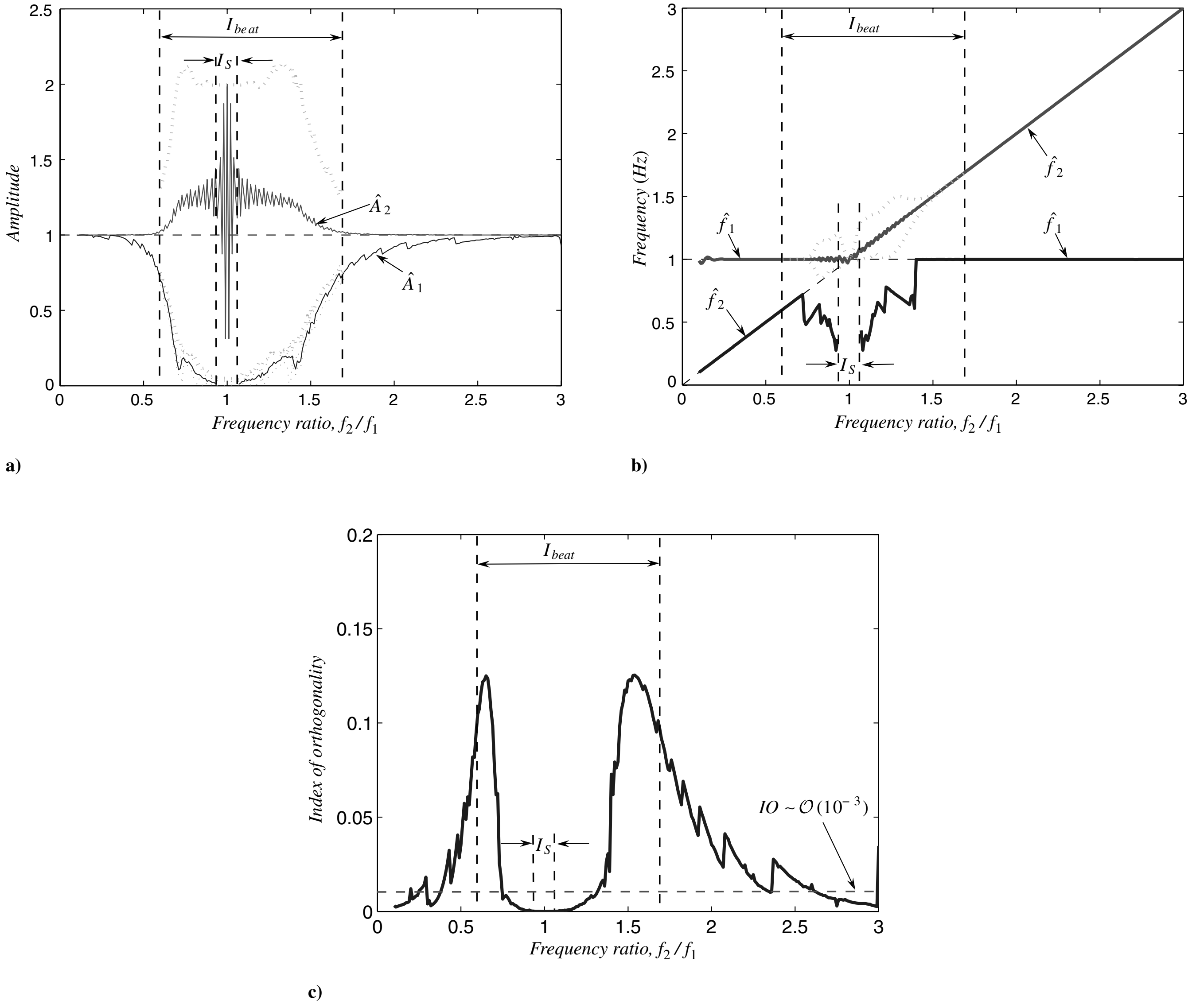

a)

b)

c)

Fig. A1 Test of EMD resolution for the signal $A_1 \sin(2\pi f_1 t) + A_2 \sin(2\pi f_2 t)$, where $A_1 = A_2 = 1, f_1 = 1$ (Hz), and f_2 varies from 0.1 to 3 Hz: a–b) amplitudes and frequencies of IMFs, respectively; (c) orthogonality index with respect to the frequency ratio f_2/f_1; solid (dotted) lines imply mean values (maximum and minimum variations); hatted quantities are computed from the corresponding IMFs.

Figure A1a depicts the amplitudes $\hat{A}_1$ and $\hat{A}_2$ of these two IMFs. If the decompositions were ideal, $\hat{A}_1$ ($\hat{A}_2$) should be the same as A_1 (A_2). However, there exist large fluctuations in the amplitudes when the frequency ratio f_2/f_1 is in the range [0.5,2], which is an indication of the occurrence of beating phenomena (or amplitude-modulated signals, as denoted by I_{beat}). In addition, close to frequency ratio 1 the EMD detects only a single IMF (denoted by I_s). Away from the interval I_{beat}, the amplitudes of the derived IMFs match reasonably well. The corresponding instantaneous frequencies are computed in Fig. A1b, where we note that the two frequency components are clearly separated in the interval away from I_{beat}. Interestingly, the orthogonality of the two harmonics becomes worse in the interval I_{beat} (Fig. A1c), except near I_s where only the single IMF is computed (exhibiting modulations) corresponding to zero index of orthogonality.

Deering and Kaiser [27] claimed that a masking signal can improve this deficiency in frequency resolution, which should be useful for intermittency (or mode mixing). Also, supplementary tools such as application of an adaptive bandpass filter [24], the wavelet packet transform [23], masking signals based on the fast Fourier transform [21], and ensemble EMD [25] can contribute toward the decomposition of closely spaced modes. However, there seems to remain a limitation in decomposing beating signals using EMD.

Acknowledgments

This work was supported in part by the U.S. Air Force Office of Scientific Research through Grant Number FA9550-07-1-0335, and in part by the grant for basic research KARATHEODORI awarded by the National Technical University of Athens, Greece.

References

[1] Mitra, S. K., *Digital Signal Processing: A Computer-Based Approach*, McGraw–Hill, New York, 1998.

[2] Nayfeh, A., *Introduction to Perturbation Techniques*, Wiley, New York, 1980.

[3] Verhulst, F., *Nonlinear Differential Equations and Dynamical Systems*, 2nd ed., Springer–Verlag, New York, 1995.

[4] Manevitch, L. I., "Complex Representation of Dynamics of Coupled Nonlinear Oscillators," *Mathematical Models of Non-Linear Excitations, Transfer, Dynamics, and Control in Condensed Systems and Other Media*, Plenum, New York, 1999, pp. 269–300.

[5] Manevitch, L., "The Description of Localized Normal Modes in a Chain of Nonlinear Coupled Oscillators using Complex Variables," *Nonlinear Dynamics*, Vol. 25, Nos. 1–3, 2001, pp. 95–109.
doi:10.1023/A:1012994430793

[6] Gendelman, O., Manevitch, L., Vakakis, A., and M'Closkey, R., "Energy Pumping in Coupled Mechanical Oscillators, Part I: Dynamics of the Underlying Hamiltonian Systems," *Journal of Applied Mechanics*, Vol. 68, No. 1, 2001, pp. 34–41.
doi:10.1115/1.1345524

[7] Vakakis, A., and Gendelman, O., "Energy Pumping in Coupled Mechanical Oscillators, Part II: Resonance Capture," *Journal of Applied Mechanics*, Vol. 68, No. 1, Jan. 2001, pp. 42–48.
doi:10.1115/1.1345525

[8] Verhulst, F., "Singular Perturbation Methods for Slow-Fast Dynamics," *Nonlinear Dynamics*, Vol. 50, No. 4, Dec. 2007, pp. 747–753.
doi:10.1007/s11071-007-9236-z

[9] Poulariskas, A. (ed.), *The Transforms and Applications Handbook*, CRC and IEEE Press, Boca Raton, FL, 1995.

[10] Huang, N., Shen, Z., Long, S., Wu, M., Shih, H., Zheng, Q., Yen, N.-C., Tung, C., and Liu, H., "The Empirical Mode Decompostion and the Hilbert Spectrum for Nonlinear and Non-Stationary Time Series Analysis," *Proceedings of the Royal Society of London, Series A: Mathematical and Physical Sciences*, Vol. 454, No. 1971, 1998, pp. 903–995.
doi:10.1098/rspa.1998.0193

[11] Huang, N., Shen, Z., and Long, S., "A New View of Nonlinear Water Waves: The Hilbert Spectrum," *Annual Review of Fluid. Mechanics*, Vol. 31, No. 1, 1999, pp. 417–457.
doi:10.1146/annurev.fluid.31.1.417

[12] Huang, N., Wu, M.-L., Long, S. R., Shen, S., Qu, W., Gloersen, P., and Fan, K., "A Confidence Limit for the Empirical Mode Decomposition and Hilbert Spectral Analysis," *Proceedings of the Royal Society of London, Series A. Mathematical and Physical Sciences*, Vol. 459, No. 2037, 2003, pp. 2317–2345.
doi:10.1098/rspa.2003.1123

[13] Yang, J. N., Lei, Y., Pan, S., and Huang, N., "System Identification of Linear Structures based on Hilbert–Huang Spectral Analysis. Part 1: Normal Modes," *Earthquake Engineering Structural Dynamics*, Vol. 32, No. 9, May 2003, pp. 1443–1467.
doi:10.1002/eqe.287

[14] Yang, J. N., Lei, Y., Pan, S., and Huang, N., "System Identification of Linear Structures based on Hilbert–Huang Spectral Analysis. Part 2: Complex Modes," *Earthquake Engineering Structural Dynamics*, Vol. 32, No. 10, May 2003, pp. 1533–1554.
doi:10.1002/eqe.288

[15] Pai, P. F., "Nonlinear Vibration Characterization by Signal Decomposition," *Journal of Sound and Vibration*, Vol. 307, Nos. 3–5, Nov. 2007, pp. 527–544.
doi:10.1016/j.jsv.2007.06.056

[16] Zhang, R., King, R., Olson, L., and Xu, Y.-L., "Dynamic Response of the Trinity River Relief Bridge to Controlled Pile Damage: Modeling and Experimental Data Analysis Comparing Fourier and Hilbert–Huang Techniques," *Journal of Sound and Vibration*, Vol. 285, Nos. 4–5, 2005, pp. 1049–1070.
doi:10.1016/j.jsv.2004.09.032

[17] Yu, D., Cheng, J., and Yang, Y., "Application of EMD Method and Hilbert Spectrum to the Fault Diagnosis of Roller Bearings," *Mechanical Systems and Signal Processing*, Vol. 19, No. 2, 2005, pp. 259–270.
doi:10.1016/S0888-3270(03)00099-2

[18] Chen, T.-l., Que, P.-w., Zhang, Q., and Liu, Q.-k., "Ultrasonic Signal Identification by Empirical Mode Decomposition and Hilbert Transform," *Review of Scientific Instruments*, Vol. 76, No. 8, Aug. 2005, pp. 085109–6.
doi:10.1063/1.2006367

[19] Zhang, Y., "Hilbert–Huang Transform and Marginal Spectrum for Detection of Bearing Localized Defects," *Proceedings of the Sixth World Congress on Intelligent Control and Automation, 2006*, Vol. 2, 2006, pp. 5457–5461.

[20] Junsheng, C., Dejie, Y., and Yu, Y., "The Application of Energy Operator Demodulation Approach based on EMD in Machinery Fault Diagnosis," *Mechanical Systems and Signal Processing*, Vol. 21, No. 2, Feb. 2007, pp. 668–677.
doi:10.1016/j.ymssp.2005.10.005

[21] Chen, Y., and Feng, M., "A Technique to Improve the Empirical Mode Decomposition in the Hilbert–Huang Transform," *Earthquake Engineering and Engineering Vibration*, Vol. 2, No. 1, June 2003, pp. 75–85.
doi:10.1007/BF02857540

[22] Flandrin, P., Rilling, G., and Gonçalvés, P., "Empirical Mode Decomposition as a Filter Bank," *IEEE Signal Processing Letters*, Vol. 11, No. 2, Feb. 2004, pp. 112–114.
doi:10.1109/LSP.2003.821662

[23] Peng, Z., Tse, P., and Chu, F., "An Improved Hilbert–Huang Transform and Its Application in Vibration Signal Analysis," *Journal of Sound and Vibration*, Vol. 286, Nos. 1–2, 2005, pp. 187–205.
doi:10.1016/j.jsv.2004.10.005

[24] Yang, W.-X., "Interpretation of Mechanical Signals Using an Improved Hilbert–Huang Transform," *Mechanical Systems and Signal Processing*, Vol. 22, No. 5, 2008, pp. 1061–1071.
doi:10.1016/j.ymssp.2007.11.024

[25] Wu, Z., and Huang, N. E., "Ensemble Empirical Mode Decomposition: A Noise-Assisted Data Analysis Method," *Advances in Adaptive Data Analysis*, Vol. 1, No. 1, 2009, pp. 1–41.
doi:10.1142/S1793536909000047

[26] Senroy, N., Suryanarayanan, S., and Ribeiro, P., "An Improved Hilbert–Huang Method for Analysis of Time-Varying Waveforms in Power Quality," *IEEE Transactions on Power Systems; IEEE Transactions on Power Electronics*, Vol. 22, No. 4, Nov. 2007, pp. 1843–1850.
doi:10.1109/TPWRS.2007.907542

[27] Deering, R., and Kaiser, J. F., "The Use of a Masking Signal to Improve Empirical Mode Decomposition," *International Conference on Acoustics, Speech, and Signal Processing: Proceedings*, Vol. 1, Inst. of Electrical and Electronics Engineers, Piscataway, NJ, 2005, pp. 485–488.

[28] Kerschen, G., Vakakis, A., Lee, Y., McFarland, D., and Bergman, L., "Toward a Fundamental Understanding of the Hilbert–Huang Transform," *Proceedings of the 24th International Modal Analysis Conference (IMAC)*, St. Louis, Missouri, 30 Jan.–2 Feb. 2006.

[29] Kerschen, G., Vakakis, A., Lee, Y., McFarland, D., and Bergman, L., "Toward a Fundamental Understanding of the Hilbert–Huang

Transform in Nonlinear Structural Dynamics," *Journal of Vibration and Control*, Vol. 14, No. 1–2, Jan. 2008, pp. 77–105. doi:10.1177/1077546307079381

[30] Lee, Y. S., Tsakirtzis, S., Vakakis, A. F., McFarland, D. M., and Bergman, L. A., "A Time-Domain Nonlinear System Identification Method Based on Multiscale Dynamic Partitions," *Meccanica* (submitted for publication).

[31] Nayfeh, A., and Mook, D., *Nonlinear Oscillations*, Wiley, New York, 1979.

[32] Vakakis, A. F., Gendelman, O., Bergman, L. A., McFarland, D. M., Kerschen, G., and Lee, Y. S., *Passive Nonlinear Targeted Energy Transfer in Mechanical and Structural Systems: I and II*, Springer–Verlag, Berlin and New York, 2008.

[33] Lochak, P., and Meunier, C., *Multiphase Averaging for Classical Systems: With Applications to Adiabatic Theorems*, Springer–Verlag, New York, 1988.

[34] Lee, Y., Kerschen, G., Vakakis, A., Panagopoulos, P., Bergman, L., and McFarland, D. M., "Complicated Dynamics of a Linear Oscillator with a Light, Essentially Nonlinear Attachment," *Physica D*, Vol. 204, Nos. 1–2, 2005, pp. 41–69. doi:10.1016/j.physd.2005.03.014

[35] Kerschen, G., Lee, Y., Vakakis, A., McFarland, D. M., and Bergman, L., "Irreversible Passive Energy Transfer in Coupled Oscillators with Essential Nonlinearity," *SIAM Journal on Applied Mathematics*, Vol. 66, No. 2, 2005, pp. 648–679. doi:10.1137/040613706

[36] Lee, Y., Vakakis, A., Bergman, L., McFarland, D. M., and Kerschen, G., "Triggering Mechanisms of Limit Cycle Oscillations due to Aeroelastic Instability," *Journal of Fluids and Structures*, Vol. 21, Nos. 5–7, 2005, pp. 485–529. doi:10.1016/j.jfluidstructs.2005.08.011

[37] Sharpley, R. C., and Vatchev, V., "Analysis of the Intrinsic Mode Functions," Industrial Mathematics Institute (IMI) Technical Repts, Dept. of Mathematics, Univ, of South Carolina, No. 12, 2004.

[38] Rilling, G., Flandrin, P., and Gonnçalvès, P., "On Empirical Mode Decomposition and Its Algorithms," *Proceedings of the IEEE-Eurasip Workshop on Nonlinear Signal and Image Processing*, Grado, Italy, June 2003.

[39] Argoul, P., and Le, T.-P., "Instantaneous Indicators of Structural BehaviorBased on the Continuous Cauchy Wavelet Analysis," *Mechanical Systems and Signal Processing*, Vol. 17, No. 1, Jan. 2003, pp. 243–250. doi:10.1006/mssp.2002.1557

[40] Le, T.-P., and Argoul, P., "Continuous Wavelet Transform for Modal Identification using Free Decay Response," *Journal of Sound and Vibration*, Vol. 277, Nos. 1–2, Oct. 2004, pp. 73–100. doi:10.1016/j.jsv.2003.08.049

[41] Delechelle, E., Lemoine, J., and Niang, O., "Empirical Mode Decomposition: An Analytical Approach for Sifting Process," *IEEE Signal Processing Letters*, Vol. 12, No. 11, Nov. 2005, pp. 764–767. doi:10.1109/LSP.2005.856878

[42] Bedrosian, E., "A Product Theorem for Hilbert Transform," *Proceedings of the IEEE*, Vol. 51, No. 51963, pp. 868–869. doi:10.1109/PROC.1963.2308

F. Pai
Associate Editor